AGU PUBLICATIONS

Earth and Space Science

RESEARCH ARTICLE

10.1002/2017EA000324

This article is a companion to Crosta et al. (2018) https://doi.org/10.1002/2017JE005398.

Key Points:
- A unique landslide inventory at planet scale is presented, introducing new landslide types, characters supporting analyses
- Statistical analysis of an inventory one order magnitude larger than previous ones conveys new understanding about landslide distribution
- Landslide triggering and environmental conditions are discussed and analyzed comparing to other data sets and terrestrial analogs

Supporting Information:
- Supporting Information S1
- Data Set S1
- Data Set S2

Correspondence to:
G. B. Crosta,
giovannibattista.crosta@unimib.it

Citation:
Crosta, G. B., Frattini, P., Valbuzzi, E., & De Blasio, F. V. (2018). Introducing a new inventory of large Martian landslides. *Earth and Space Science*, *5*, 89–119. https://doi.org/10.1002/2017EA000324

Received 25 JUL 2017
Accepted 20 FEB 2018
Accepted article online 1 MAR 2018
Published online 13 APR 2018

©2018. The Authors.
This is an open access article under the terms of the Creative Commons Attribution-NonCommercial-NoDerivs License, which permits use and distribution in any medium, provided the original work is properly cited, the use is non-commercial and no modifications or adaptations are made.

Introducing a New Inventory of Large Martian Landslides

G. B. Crosta[1], P. Frattini[1], E. Valbuzzi[1], and F. V. De Blasio[1]

[1]Department of Earth and Environmental Sciences, Università degli Studi di Milano Bicocca, Milano, Italy

Abstract Landslides have been observed in different terrestrial environments and also on planets, satellites, and asteroids. Long runout landslides are strongly dependent on the initial mass position, material and slope path properties, topographic relief, and presence of volatiles. Therefore, landslides represent a means for the description of rock properties and environment of deposition prevailing at the time of occurrence and may assist in understanding the geological and climatological history of the planetary surfaces. Concerning Mars, previous studies have concentrated on Valles Marineris, where among the largest and longest landslides have been observed. Using different imagery, we present and analyze an original database of 3,118 Martian landslides of deposit area greater than 0.1 km^2 throughout the planet between 60°N and 60°S, resulting in a data set far richer than previously done. After a distinction is made between different typologies of landslides, their position and the statistical distribution of their geometrical properties are examined. Large landslides cluster along the Noctis Labyrinthus-Valles Marineris-Margaritifer Terra system. Rock avalanches within craters are widespread, but no significant large landslides have been found at latitudes higher than 40°S and 46°N. The magnitude-frequency distribution follows a power law with scaling exponent ranging between 1.02 and 1.57, for the entire data set and varies according to the geomorphological settings, the landslide typology, and mobility. A volume-area power law relationship (exponent: 1.12–1.24) is proposed, based on the reconstruction of 222 landslide geometries, and compared to those for similar terrestrial landslides (1.39). Similarities with respect to terrestrial landslide, distribution with respect to impact craters and impact energy, and cryosphere extent are also discussed.

Plain Language Summary Landslides are geomorphological phenomena that can strongly control the evolution of a landscape. They have been observed in different environments on planets, satellites, and asteroids. Landslides are sensitive to rock strength, slope geometry, and geological and environmental conditions and to their perturbations. Long runout landslides are characterized by exceptional runout and are dependent on the material and slope path properties, path geometry, presence of ice, water, liquefied soil, and vapor. Therefore, they can spread light over the conditions existing at a specific site or region or even a planet. Martian landslides are the best preserved in the whole solar system. We present and analyze an original database of about 3,100 Martian landslides spread throughout the whole planet. We study the position of landslide types and the statistical distribution of their geometrical properties, from which details of the rock material and the possible triggering and landslide dynamics can be inferred. Rock avalanches within craters are widespread in the planet, but no significant large landslides have been found at latitudes higher than 40°S and 46°N. Similarities with respect to terrestrial landslides, distribution with respect to impact craters and impact energy, and cryosphere extent are also discussed.

1. Introduction

Following the widely used definition of Varnes (1978), landslides are "downward and outward movement of slope-forming materials composed of natural rock, soils, artificial fills,—or combinations of these materials." Landslides are relevant geomorphological processes that occur in very different environmental conditions, developing under fully subaerial or subaqueous conditions or at the transition between the two. The environmental conditions play a major control on the triggering factors, the most frequently described ones being rainfall, earthquake shaking, rapid snowmelt, strong temperature changes and fracture ice deterioration, volcanic activity, undercutting and oversteepening, and human actions. If all these hold true, then landslides occurring in the same area, or under strictly the same average controlling and triggering conditions, should have similar characteristics. As a consequence, preparing a landslide inventory map should help at understanding the environmental, geomorphological, and geomechanical conditions at the time of triggering and eventually also to recognize landsliding events that occurred at different times or under changing conditions. All these issues have been considered as valid for landslide studies both on Earth and on other

planets. Because landslides are sensitive to rock, slope, geological, and environmental conditions and considering that they can maintain their aspect after billions of years, in absence of erosion and masking factors, the examination of landslides may assist understanding the geological and climatological history of the planetary surfaces. Since the early Viking images and the seminal work of Lucchitta (1979), various researchers have provided inventories of Martian landslides, which have progressed with time in quality and extent as better probes were becoming available. To our knowledge, the most significant in terms of breadth and number of reported cases have been exposed in early works (Lucchitta, 1979; Lucchitta et al., 1992; McEwen, 1989; Quantin, Allemand, & Delacourt, 2004; Quantin, Allemand, Mangold, et al., 2004; Shaller, 1991) and in the more recent compilations (Brunetti et al., 2014; Bulmer, 2012; Crosta, Frattini, & Valbuzzi, 2013; Grindrod & Warner, 2014; Stucky de Quay & Grindrod, 2014). Most of these inventories focused on the Valles Marineris (VM), which is located in the equatorial region of Mars. In the work by Lucchitta (1979), a total of 35 large landslides were resolved on Viking images. Shaller (1991) reported 104 landslides within and 47 landslides outside of VM boundaries (mainly between 30°N and 30°S), respectively, mapping phenomena quite similar to those more recently mapped by other authors in the VM area. He also compared these landslides to 221 terrestrial landslides. Crosta, Frattini, and Valbuzzi (2013) quote an inventory of 1,200 landslides; Brunetti et al. (2014) identified and mapped 219 mass wasting features among rockslides, complex/compound failures, rock avalanches, and debris flows, of which 21 are putative rock glaciers.

The VM area is characterized by a complex system of canyons or Chasmata, whose origin is discussed in various works (e.g., Andrews-Hanna, 2012a, 2012b, 2012c; Carr, 1996; Lucchitta et al., 1992; Watkins, Ehlmann, & Yin, 2015; Yin, 2012). VM slopes have a relatively simple geometry characterized by a rise, 6–10 km high, with almost constant slope gradient (15°–30°) and two upper and lower flat sectors. A series of gravitational instabilities classified roughly as large slumps and long runout landslides, up to several hundred cubic kilometers in volume, affect these slopes. The large scars, suspended above the valley bottom, are often juxtaposed in long series with associated multiple failures of variable characteristics. Landslides in VM are very well-preserved features that captured the planet surface at the instant of failure; also because of this, the visible landslide deposits often show the superposition of multiple events. Landslide age is defined in a relative way based on the appearance of the main observable features. Absolute landslide dating accomplished by crater count chronology (Quantin, Allemand, & Delacourt, 2004) shows that landslide events occurred over a very large time interval roughly embracing 3.5 Gy. More recently, Grindrod and Warner (2014) and Hager and Schedl (2017) found an age interval between 0.1 and 3.4 Ga revealing large age differences (0.2 to 1.8 Ga) with respect to ages by Quantin, Allemand, Mangold, et al. (2004) and suggesting (Grindrod & Warner, 2014; Warner et al., 2015) the need for crater counting to cover larger areas. It is clear that such long-time span could involve different environmental conditions on the planet and different controlling and triggering factors for landslides. Therefore, their analysis can disclose environmental and geologic information useful for the reconstruction of the planet history. Nevertheless, landslides in VM are only a part of those actually observable on the planet surface. To overcome this bias in the mapping, description, and analysis of the characters of mass movements on Mars, we compiled a new inventory covering a large extent of the Martian landscape.

To accomplish this analysis and to compare the observed phenomena to the earth analogs, the peculiar characteristics of Mars must be taken into account. Gravity is about one third (3.71 m s^{-2} on average) that on Earth, the atmosphere is prevalently composed by CO_2 (95.32%), and the surface temperature ranges between 186 and 293 K. Furthermore, Mars surface is affected by both ice and water erosion and deposition forms (Colaprete & Jakosky, 1998; Hubbard et al., 2014; Kargel, 2004). Glacial and periglacial features are frequent at high latitudes (Souness et al., 2012), and their comparison to terrestrial equivalents suggests a progressive change in environmental conditions (Laskar et al., 2004). The hypothesis behind this is that availability of a large data set covering different terrains, located in different materials, at different altitudes, latitudes, and longitudes might help at reaching a better understanding of the mechanics, involved processes, and controlling factors. Lucchitta (1987) and Shaller (1991) discussed the possible effects of water and ice on Martian landslide evolution. Shaller tried a separation among dry (also termed dry Blackhawk-like landslides), moist, and wet (i.e., saturated) landslides based on mainly a few morphological features. He noticed that most of the dry-like landslides were located outside VM and that they occurred essentially under current Martian environmental conditions, whereas many moist ones were located within VM.

The stability of the VM rock slopes, involving the instability mechanisms and triggering perturbations, has been examined in the literature (e.g., Bigot-Cormier & Montgomery, 2007; Crosta, Frattini, & Agliardi, 2013; Lucas et al., 2011; Neuffer & Schultz, 2006; Schultz, 2002). These analyses help at constraining the mechanical properties of the rock, the presence of water, ice, clay, and evaporites (e.g., Crosta, Utili, et al., 2013; De Blasio, 2011a, 2011b; Harrison & Grimm, 2003; Shaller, 1991). It appears that impact cratering processes have been important in determining many of the landslides not only by seismic shaking of the ground (Crosta, Utili, et al., 2013) but also as a predisposing factor through the process of impact gardening (Frattini et al., 2014).

Although the mentioned references (Brunetti et al., 2014; Bulmer, 2012; Crosta, Frattini, & Valbuzzi, 2013; Grindrod & Warner, 2014; Stucky de Quay & Grindrod, 2014) have continuously updated the inventory of Martian landslides, there is need for a database that considers landslides not only from special regions of the planet (most often VM) but also in their global distribution around the planet. Moreover, the number of considered landslides is so far too scarce to be representative when considering landslides and their geometrical characteristics in a statistical sense. This is particularly true when analysis should be performed of landslides characteristics comparing different areas of the planet or different landslide typologies. In this work, we thus present an inventory of unprecedented number of landslides (3,118), comparable and actually outcompeting similar landslides databases for the Earth.

The paper is structured as follows: a description of the methods and criteria adopted for the mapping and classification is presented; a statistical analysis of the landslide distribution and characteristics is performed, and results are presented. A discussion of all the data presented is prepared in the light of the available literature to suggest possible use and interpretation of this data set as a supporting information for environmental studies and to analyze the evolution of the planet Mars. The possible relationship to impact craters distribution and to the extent of the cryosphere is discussed together with the similarities to terrestrial landslides. A detailed description of the inventory attributes is presented in the supporting information.

2. Methods

2.1. Data Gathering From Image Databases

Available data and images now covering most of the Mars surface have been studied in detail, building a GIS geodatabase for the mass movements on Mars. These consisted of visible image data sets including High Resolution Stereo Camera on Mars Express (HRSC) 18 m/pixel images (Neukum et al., 2004), Mars Orbital Camera 1.5 to 12 m/pixel images, Context Imager 5 to 6 m/pixel images, and locally HiRISE at 0.3 m/pixel images (Malin et al., 2007). Since 2009, Google Earth™ includes a separate globe of the planet Mars as a 3D tool encompassing Viking, Mars Orbital Camera, HRSC, HiRISE, and Context Imager images. All these mosaic images are superimposed on a 3D topography derived from 400 m gridded Mars Orbiter Laser Altimeter (MOLA; Smith et al., 1999). This allows a rapid 2D and 3D visualization and direct images retrieval by connecting to the data repositories. HRSC-derived DEM with a grid-cell resolution of 50 to 150 m, available from the Mars Express HRSC image archive at the Freie Universitaet Berlin (http://hrscview.fu-berlin.de), have been used for elevations and to derive the morphological parameters of 74% of the landslides. For the other 26% of the landslides, MOLA DEM with a grid-cell resolution of 463 m has been used. The latter DEM shows a smoothing of the surface, resulting in slope angles that are underestimated with respect to the actual ones. However, given the large size of Martian landslides, this smoothing does not affect the analysis significantly, especially regarding the landslide mobility.

2.2. Landslide Mapping

Landslides have been recognized and mapped according to standard geomorphological criteria, such as the presence of scars associated with recognizable deposits at the toe, the presence of morphostructures within the deposit suggesting displacement (e.g., ridges, hummocky surfaces), the presence of lateral levees, the geomorphological evidence of slope deformation and displacements along individual structures, and the subdivision in multiple confining or nested elements, with clear lateral interruption or when considered really significant in terms of extent or possible evolution of the phenomenon. For each landslide, the scar, transport, and accumulation limits have been mapped on Google Earth, imported in ArcGis™, edited based on shaded relief for shape improvement, and eventually organized into a GIS geodatabase. Three senior scientists experienced in landslide mapping in different environments carried out independently the mapping by

combined use of images of different characteristics. Mapping has been done systematically for the entire planet between −60° and 60° in latitude, applying a minimum threshold value of about 0.1 km^2. Polar areas have been excluded also because they are almost completely covered by ice. Other phenomena of mass wasting such as dark stripes or seasonal flows, rock falls, debris flows, and slumps inside craters have not been mapped in the present work. Landslides have been searched by analyzing areas with large relief along morphological scarps, main and secondary valleys, and volcanic edifices (e.g., Olympus Mons, Tharsis, and Elysium). Then, landslides within craters have been analyzed with the aid of Robbins and Hynek (2012) crater inventory. In this inventory, Robbins and Hynek (2012) reported 13,696 craters with diameters larger than 1 km and characterized by the presence of slumps and flows. In our inventory, this set of craters from Robbins and Hynek (2012) has been analyzed in detail to attain a complete mapping of flow-like landslides as polygons. Slumps as from their inventory (always within craters and always only as a yes or no attribute) are reported in Figure 1 and have been used only to observe their regional distribution. Our novel data have been compared with previously published data sets both for completeness of the data set and for comparison of classification and interpretation. Possible undersampling of the landslides might be originated from the availability of high-resolution images, the coverage of the planet surface, and interpretation bias.

A preliminary data set (Crosta, Frattini, & Valbuzzi, 2013) is detailed and largely extended here. One of the novelties of the present inventory consists in the inclusion of an unprecedented number of landslides (3,118), which allows a robust statistical study comparable with similar landslide databases for the Earth (Figure 1 and Figures S1 to S8 in the supporting information).

2.3. Inventory Attributes

In this study, each landslide mapped within the data set has been classified according to the different criteria:

1. **Landslide portion:** scar (N), deposit (A), block (D)
2. **Type of landslide:** rock avalanche (RA), slump (S), slump/rock avalanche (SRA), debris flow (DF), rock avalanche/ejecta (RAEJ), spreading/sagging/deep-seated gravitational slope deformations (DSGSD; (DS) mapped in another shape). A thorough description of different landslide types is reported in section 3.
3. **Geomorphological setting:** main valley (MV), secondary valley (SV), chaos (CH), affecting volcano flanks (OV), within volcanic caldera (IV), within crater (IC), along the outer side of an impact crater (AOC), within crater border due to impact (AIC), labyrinth (L), northern plains/dichotomic line (P)
4. **Geographical region:** Alba Patera (ALBA), Arabia Terra (ARAB), Terra Cimmeria (CIMM), Elysium Mons (ELYS), Ganges Chasma (GANG), Juventia Chasma (JUVE), Kasei Valles (KASE), Lunae Planum (LUNA), Margaritifer Terra (MARG), Noachis Terra (NOAC), Noctis Labyrinthus (NOCT), Olumpus Mons (OLYM), Promethei Terra (PROM), Terra Sabaea (SABA), Shalbatana Vallis (SHAL), Terra Sirenum (SIRE), Tharsis Montes (THAR), Tyrrhena Terra (TYRR), Xanthe Terra (XANT), and Valles Marineris (VM), which is in turn subdivided in Candor Chasma (CAND), Coprates Chasma (COPR), Eos Chasma (EOS), Hebes Chasma (HEBE), Ius Chasma (IUS), Melas Chasma (MELA), and Tithonium Chasma (TITH)
5. **Landslide deposit shape:** apron-like (A), elongated (E), rectangular (RL)
6. **Number of scars:** single scar (SS), complex/multiple scars (MS)
7. **Degree of confinement:** unconfined (NC), partially confined (PC), confined (C)
8. **Type of confinement:** frontal (F), frontal with runup (FR), lateral right (LR), lateral left (LL), bilateral (B), frontal with runup and reflection (RR), frontal and bilateral (BF)
9. **Material distribution within the deposit**: upper landslide sector (HS), homogeneously distributed (OD), at the front (OF)
10. **Relationship with other landslides:** independent (OL), inside larger landslide (IL)
11. **Scar shape:** circular (CS), rectangular (RS), triangular (T), crater (CR)
12. **Deposit characteristics:** longitudinally striated (SL), transversally striated (ST), hummocky (H), hummocky with striations (HSL), stepped (G), indistinguishable (I); striations: means with grooves and furrows of different orientation
13. **Number of lobes:** single lobe (SL), multiple lobes (ML)
14. **Presence of levees:** with levees (LE), without levees (NLE)
15. **Reliability and type of uncertainty:** uncertain scar (US), uncertain deposit (UD), uncertain landslide (UL), certain landslide (C).

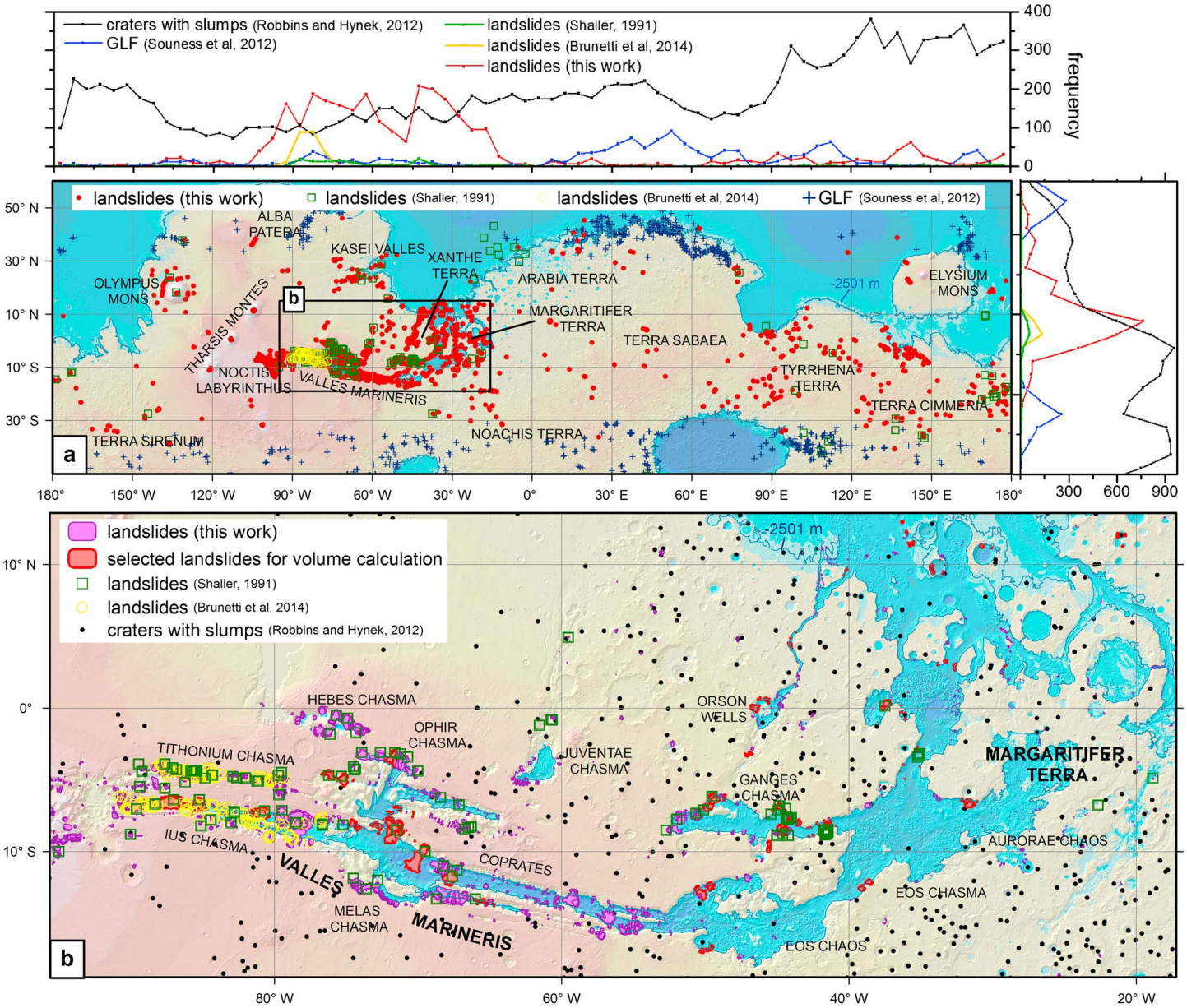

Figure 1. Martian landslides inventory. (a) Landslide locations as points compared with previous landslide inventories (Brunetti et al., 2014; Shaller, 1991) and glacier-like forms (GLF; Souness et al., 2012). The side plots report the frequency of landslides, GLF, craters with slumps (Robbins & Hynek, 2012), and landslides from previous inventories as a function of longitude (top panel) and latitude (right panel). DEM is colored according to elevation and shaded relief. The ocean level (−2,501 m; Di Achille & Hynek, 2010) is reported as a blue line. (b) Detail for the Noctis Labyrinthus-Valles Marineris area with landslides of the inventory reported as polygons. Selected landslides used for pre-event topographic reconstruction are reported. Craters with slumps according to Robbins and Hynek (2012) are reported as points. See Figures S1 to S8 in the supporting information for more detailed maps.

Multiple accumulations from the same source area or from different sources have been differentiated where possible to obtain a more complete data set. The landslide type classification and criteria that have been adopted for the preparation of the inventory are introduced in the following (see supporting information for attributes details).

2.4. Reconstruction of Prefailure and Postfailure Morphology

A complete reconstruction of the prefailure slope geometry and of the failure surface has been accomplished for a subset of major mapped landslides (Figure 1b) with the main purpose of determining their volume with maximum possible precision. The reconstruction of the prefailure geometry has been

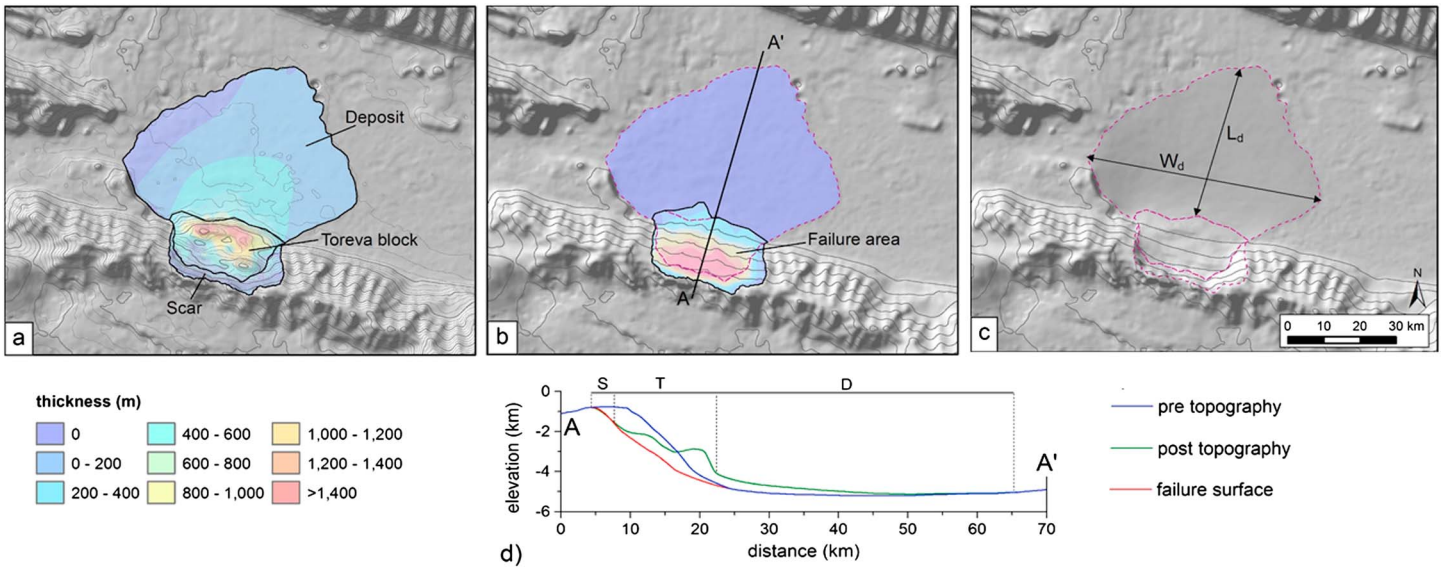

Figure 2. Example of computation of the landslide volume by reconstructing the failure surface and the prefailure topography for a landslide in the Coprates Chasma. (a) Actual topography and thickness with respect to failure surface, (b) reconstructed predeposition topography and thickness with respect to failure surface, and (c) reconstruction of the failure surface geometry. The landslide volume amounts to 640 km^3 and 518 km^3 from the niche reconstruction and the deposit geometry, respectively. These values are comparable to the volume estimated by Lucas et al. (2014) for the same landslide (540–730 km^3). Computed average thickness of the deposit is 399 m.

obtained by extrapolation of the neighboring slopes and in many cases of the upper plateau sector. To this purpose, we have selected landslides on step-like slopes and well developed and recognizable main scarp. A total of 222 landslides, all of which are rock avalanches, have been reconstructed by choosing landslides clearly identifiable in the topography and with neat deposit boundaries so that a reliable computation of the volumes can be safely accomplished. These landslides range in volume between 3×10^7 and 2×10^{12} m^3.

We proceeded as follows: First, we extracted the DEM topographic data (MOLA and/or HRSC) and generated elevation contour lines; in order to identify the scar area, we spotted sharp and evident morphological features (i.e., lineaments, scarps, slope, and surface) and identified features that have been probably affected by the mass movement (e.g., truncated and dislocated features). Once the scar was mapped, we proceeded to map the deposit. While in several examples, the deposit boundary is evident, in dubious cases we identified untouched topography or topography not covered by the landslide deposit.

Finally, we drew prefailure 50 m contour lines (except for smaller landslides) mimicking those in the neighboring areas, both over the scar and below the deposit (Figure 2). This reconstruction allowed the calculation of both the initial failure volume (i.e., volume of the generated scar) and of the final deposit volume. Calculation of the volumes has been carried out by integrating the height differences with respect to the basal area.

3. Landslide Types

3.1. Classification of Martian Landslides

As stated above, a long series of attributes has been collected and assigned to each mapped feature in the inventory. In the following, the adopted landslide type classification is detailed. The description of each landslide type also includes some of the major associated attributes that are considered fundamental for a correct classification and for a possible interpretation of the mechanisms and processes involved in the failure and propagation of the mass wasting. Six main classes of landslides, following the commonly proposed classifications (Cruden & Varnes, 1996; Hungr et al., 2014), have been recognized. Here each type of landslide is introduced according to general criteria and details adopted for their recognition and description and considered as typical or specific of many of the mapped Martian landslides.

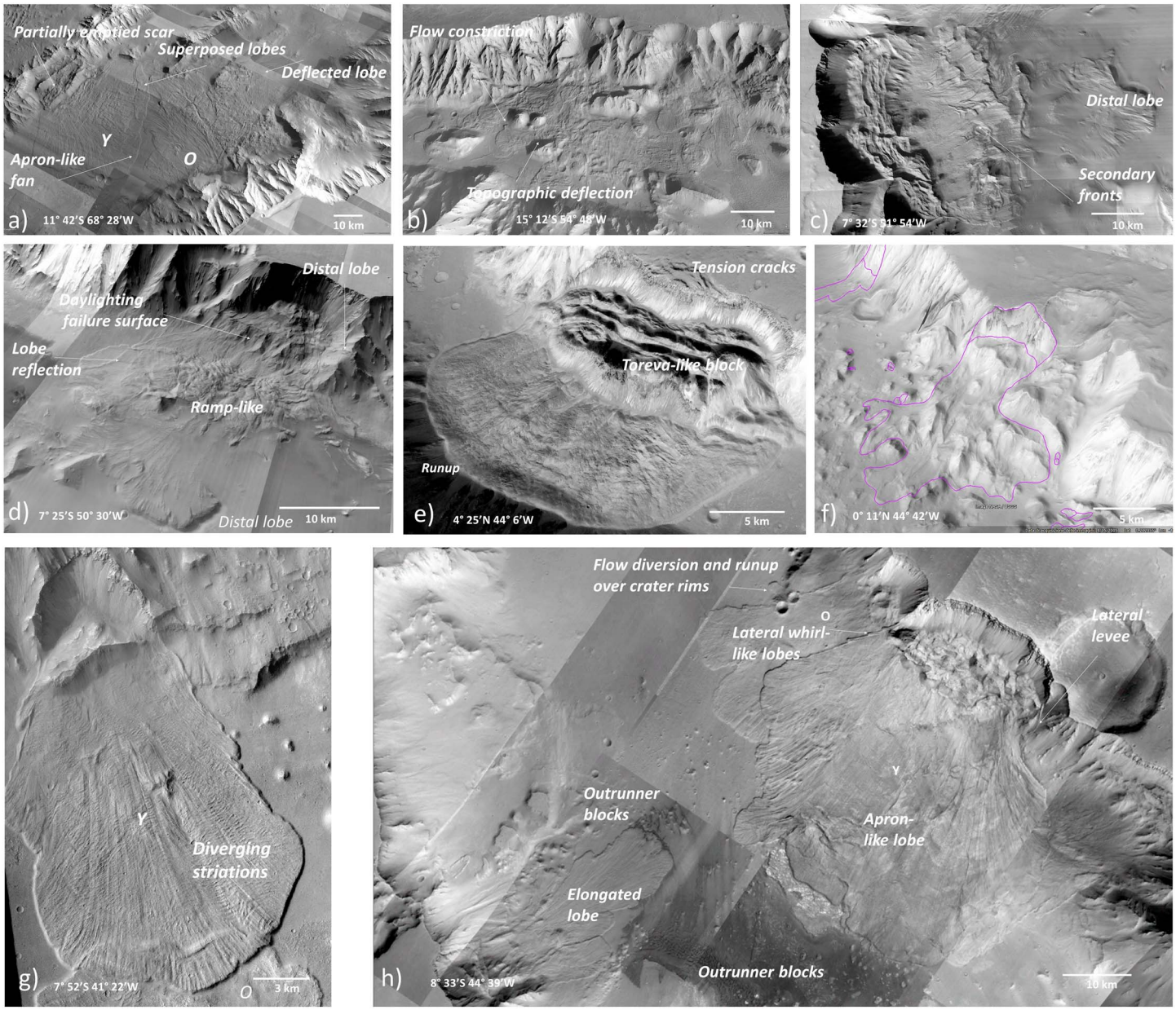

Figure 3. Types of landslide: (a) Rock avalanche with large symmetrical apron-like lobe overruning an opposite landslide deposit; (b) rock avalanches producing multiple lobe deposits with flow deflection and channeling around large mounds located at the valley bottom; (c) rock avalanche with a sharp scarp only partially emptied. Large secondary lobes characterized by sharp striations and raised bulging fronts are recognized. Main distal lobe partially masked by Aeolian deposits. (d) Large rock avalanche with multiple secondary flows, distal striated and divergent lobes, and ramp-like features. Lateral levees are visible high along the left-hand side of the source area. (e) Rock avalanche-slump with stretched front that reached to the opposite valley side and ran up the valley wall. Note the large Toreva block and the frontal lobe protruding and thinning out along the valley. (f) Rock avalanche characterized by large blocks partially removed from the source area and displaced down in the main valley bottom. (g) Rock avalanche with an elongated lobe, overrunning an antecedent rock avalanche lobe in the distal part. Transversal and longitudinal systems of ridges and furrows are visible, opening outward with distance and bending in proximity of the front. The lobe shows a sharp border. (h) Cluster of rock avalanches with elongated (lower left corner) and apron-like deposits (right-hand side) diverging from a partially emptied source area. Lobes superposition, possible out-runner blocks, and flow deflection are observed. Y and O labels stay for younger and older deposits.

3.1.1. Rock Avalanches

Rock avalanches (RA) are long runout flow-like landslide (Hungr et al., 2014) with very peculiar features characterizing their deposits. Their mobility, quantifiable with the apparent friction coefficient H/L, where H is the vertical drop height and L is the horizontal runout distance (measured from the uppermost crown point to the most distal deposit tip), is noticed to decrease quite dramatically with volume (Scheidegger, 1973).

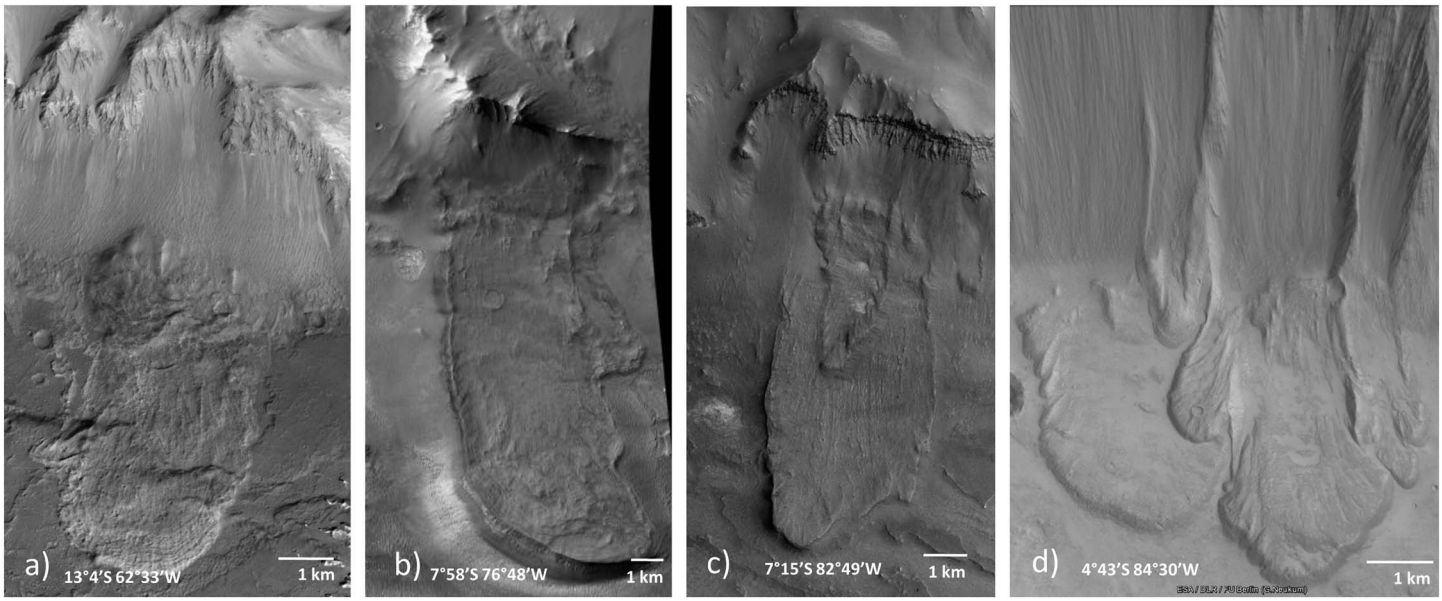

Figure 4. Different types of rock avalanche deposits characterized by presence of relatively shallow scars, with a minor curved scarp and elongated deposits with longitudinal striations, steep front, and lateral levees. They suggest failure within strongly weakened rock masses and regolith deposits. See Figure S9 (in the supporting information) for more examples.

Figure 3 shows some examples of rock avalanches on Mars. Their size can be extremely variable; while their lowermost extreme is represented by large rockfalls, the largest rock avalanches on Mars may often reach the astounding volume of 10,000 km^3, against some tens of cubic kilometers on Earth (Erismann & Abele, 2001).

Among the typical observed features, we can list longitudinal and transversal grooves and furrows, hummocky terrains, lobes, lateral levees, and ramp-like or thrust-like features. From a geometrical point of view, they are strongly elongated with evident scars completely or almost completely emptied. Where possible, the source, transit, and deposition sectors have been recognized and mapped. The deposits can be zoned, for example, in a proximal area characterized by large Toreva blocks (Reiche, 1937), which are followed downslope by long and sometimes wide lobes (e.g., Figure 3e). Toreva blocks are large masses, still preserving their internal stratigraphy, which moved along curved (listric-like) planes remaining close to or slipping away at large distance from their source. The Toreva block is generally thick whereas frontal lobes are much thinner. Observation of some of the lobes deposited in front of the Toreva blocks suggests that these lobes might be the result of frontal instabilities affecting the Toreva blocks itself.

Even in the presence of the Toreva blocks, some lateral levees deposited along the original slope at the flanks of the main scar have been recognized. These features suggest a detachment of material from the side of the Toreva blocks since their initial dislocation or the possible frontal instability of the material subsequently deposited in the frontal lobes (Figure 3e).

Typical of many Martian rock avalanches is the presence of multiple lobes, both developing juxtaposed (i.e., laterally confining) or superposed (i.e., covering each other), with strongly varying size (i.e., comparable size or very different; Figure 4). The relationships among the different lobes cannot always be resolved with a sufficient degree of certainty, and it is difficult to establish if they have been deposited in a strict temporal sequence or in a long series of isolated phenomena. In some cases, multiple large slump blocks are recognized just within or below the main scarp, isolated by concave downslope planes and cut by linear or curved features placed in an anastomosed geometry. In other cases, the blocks are not in direct physical contact among them but dispersed in a chaotic way and originating isolated mounds (e.g., Figure 3f). Because of their long runout and spreading, these landslides can be confined by the existing topographic features affecting both their shape and spreading. Secondary rock avalanches have been mapped, which develop from the scar of the main events. These secondary landslides can mask the inner or more proximal part of the deposits of the initial and larger rock avalanches. All these features are not mutually exclusive, and many of them can be found together and at different positions within the same landslide deposit. Superposition of the deposits

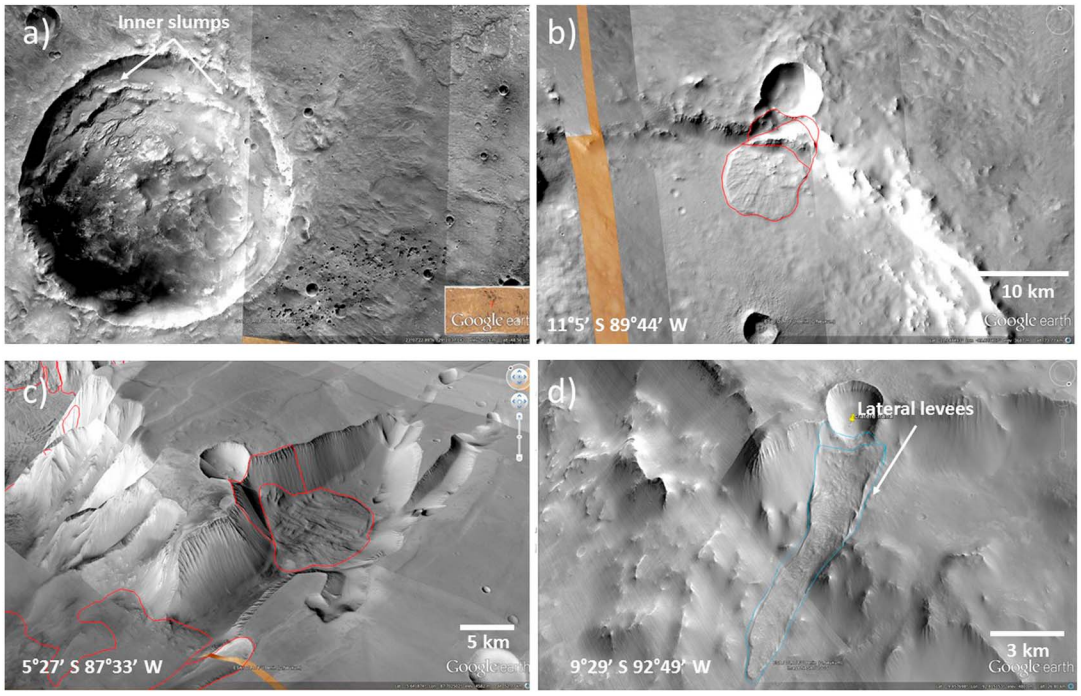

Figure 5. Landslide types associated to impact craters: (a) slumps generating a step-like geometry with concentric scarps and block displacement toward the crater center; (b–d) landslides directly associated with impacts located in proximity of slopes and valley flanks.

can be easily recognized at some places, via the evidence of superimposed lobes, or even the degree of conservation of the lobes and the number of impact craters. In general, the lobes typology can be furtherly subdivided on the basis of the characteristics of their margins: regular lobe edge, bulged front with radially oriented ridges, festoon-shaped edges (i.e., with a series of curled multiple features), lateral levees with small regularly spaced curls, multiple fronts with a sort of fingered geometry, or strongly curved margins (see Figures S10 and S11 in the supporting information).

Special cases of elongated flow-like features are those characterized by poorly defined internal structures within the frontal lobe, well-defined levees with no internal deposition. These phenomena are however associated to a clear scarp and lack completely the typical internal structures of the rock glaciers (i.e., pressure ridges and depressed lobe; Barsch, 1996; Hamilton & Whalley, 1995; Whalley & Azizi, 2003).

Finally, impact-induced landslides (Figure 5) triggered by the impact of a meteoroid on the sloping ground or valley flank or just at the upper slope crest have been recognized and mapped as independent phenomena. This new class of landslides has different characteristic features and is more mobile than other landslides in similar conditions.

3.1.2. Slumps

Slumps (S) are rotational slides of variable geometry that affect masses of rock and soil moving on curved or complex failure surfaces with a low structural control (Figure 6a). They are characterized by a much smaller runout and spreading with respect to rock avalanches. Their deposits are thicker and convex, with no clear flow features, more abundant hummocky geometry, and presence of secondary scarps (creating sometimes a stepped surface). The scar geometry is usually convex in shape, both in plane and transversal view, and the landslide head can be characterized by a back-tilted surface. In a few cases, the scarp is characterized by a rectilinear geometry and seems controlled by the linear depressions (trenches), which border or are parallel to the main valley axis, especially along the VM flanks. Their length is quite variable from a few hundreds of meters to tens of kilometers. A specific type of these phenomena is associated to the instability of the crater rim and generates a stepped geometry from the crater rim toward the inner crater (e.g., Figure 5a). Because of their abundance, not all of those present in the impact craters have been mapped. To this aim and for their analysis, the information presented in Robbins and Hynek (2012) impact crater inventory can be used.

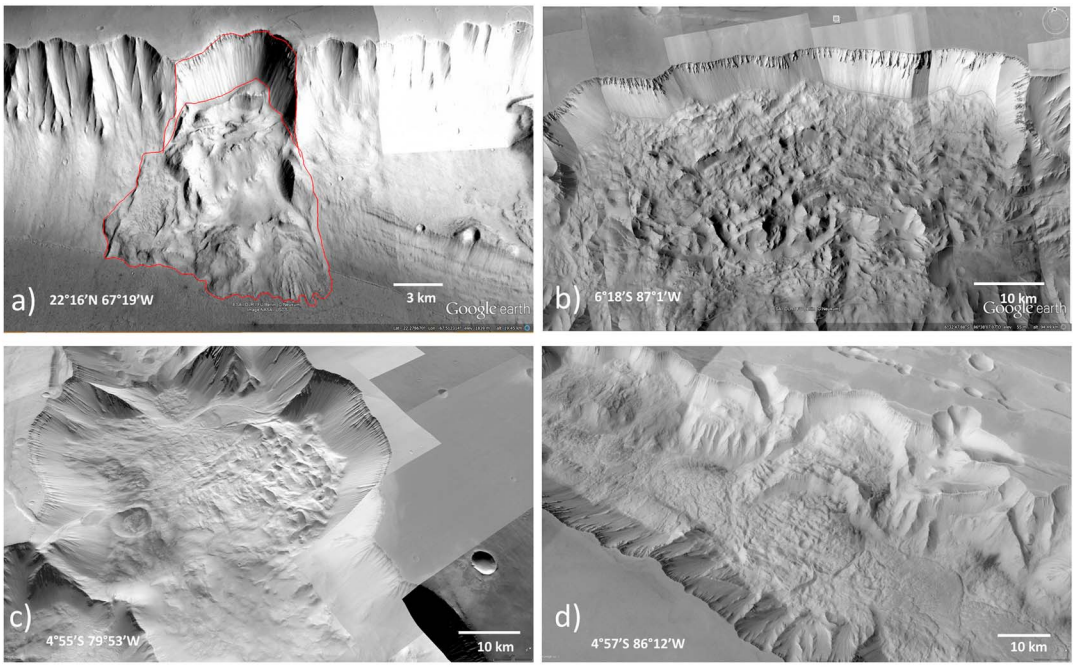

Figure 6. Types of slump and slump-flows: (a) slump where the displaced mass maintains a certain coherence and the scar is only partially emptied; (b) large multiple slumps with coalescence of different contiguous failures. The upper main scarp suggests possible control by linear features; the hummocky and crested surface of the deposit with back-tilted blocks support the idea of rotational failure surfaces with a strong horizontal component; (c, d) slumps and slump/flows characterized by partial emptying of the failure zone and different degree of confinement by opposite valley flank. Runup and leaning of the deposit on the opposite valley flank is visible. Secondary collapses within the deposits and developing along the valley axis are observed in (c) to (d). In all the cases, the deposit maintains a relevant thickness. Finally, quite peculiar phenomena for their geometry and development are those associated to the lower scarp around Olympus Mons. In this specific case, we distinguished between slumps and large rock avalanches associated to the Olympus Mons aureolae.

3.1.3. Slump/Flows

Slump/flow phenomena (S/RA) show intermediate characteristics between rock avalanches and slumps (Figure 6b). The geometry of the failure surface is similar to the one previously described. At the base of the main scarp, abundant debris deposits that partially cover the landslide head are found. The deposit is characterized by extremely variable morphologies. In general, deposit is convex with a quite chaotic/hummocky surface and some limited or less defined sectors similar to rock avalanches. In some cases, it seems that these landslides are characterized by a failure surface gently inclined downslope and daylighting in the middle of the affected slope. Above the daylighting zone, the failure resembles more a sliding and slumping (on flat like surfaces), whereas downslope the movement becomes more similar to that of a flow; in some cases, a real rock avalanche lobe is generated along the basal plain.

3.1.4. Debris Flows

The presence of debris flow (DF) deposits on Mars with all the typical features of terrestrial analogues has already been described in the literature (Johnsson et al., 2014; Lanza et al., 2010; Malin & Edgett, 2000; Tanaka, 1999). DFs show lateral levees, elongated deposits mostly developed along channels or rills, with a lobate form that generally is located on fan-shaped deposits (Figure 7a). At the outlet of secondary tributary valleys or along talus slopes, debris flows are characterized by one or more source zones, which converge in a single narrow channel or transportation sector, followed downstream by a deposition area characterized by a low topographic gradient. The deposits suggest a lateral and longitudinal migration in the depositional area and the succession of depositional events. The mapping of these features is relatively complicated because of their size and number. Therefore, only the largest and more evident ones have been mapped. In some cases, special features associated to debris flows are narrow dark stripes with a localized source very frequently observed within the crater rims (Figure 7b; Sullivan et al., 2001). Interestingly, they are usually originated very high along the internal crater slopes close to the crater rim. Some laterally well-developed flow-like deposits have been recognized below steep rocky faces and sometimes described in the literature as brine flows (McEwen et al., 2013). They are characterized by a series of adjacent flows each one characterized by small levees and frontal lobes. In some other areas, large flat cones have been mapped at the outlet of small valleys

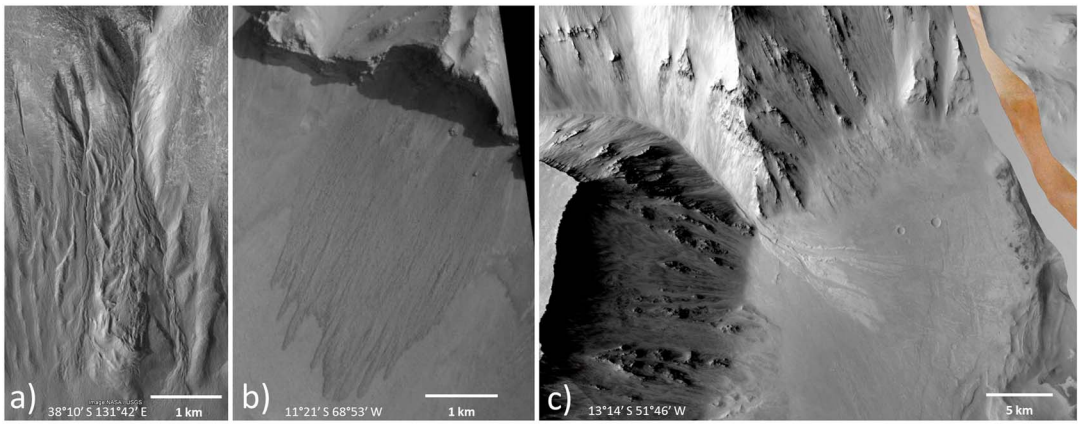

Figure 7. Example of three type of debris flows: (a) multiple debris flow deposits at the outlet of a small valley, coordinates 38.12°S, 131.7°E; (b) shallow adjacent flows at the base of a steep rocky cliff (brine flows); (c) debris flow on a gentle alluvial fan deposit at the outlet of a tributary valley.

(e.g., Gale crater; Figure 7c). They appear relatively thick, with both longitudinal and transversal structures, successive to some slumps located in the immediate proximity as suggested by their sealing effect on the slump structures.

3.1.5. Rock Avalanches/Ejecta

Rock avalanche/ejecta (RA/EJ) type features are landslides originating at the impact crater rims. Although they exhibit landslide-like behavior and have traveled down the local slope, they also share many features with impact crater ejecta (Barlow & Perez, 2003; Weiss & Head, 2013). They are characterized by well-defined tongue-shaped deposits, which resemble rock avalanche deposits. In general, the source scar is clearly distinguishable because it affects and interrupts the crater rim continuity, and this is the major feature suggesting a classification as landslide. In some cases, the deposit elongation is extremely pronounced with respect to the initial drop height (i.e., crater rim relief). The main groups of features classified in this category are those located in the Aeolis Mensae region. Figure 8 shows some examples of RA/EJ. The landslides proceeded along the preexisting channels not only driven by the gentle slope there but also as consequence of the initial velocity acquired by the ejecta. Note the presence of longitudinal furrows indicating the flow nature and direction.

3.1.6. Sagging/Deep-Seated Gravitational Slope Deformations

The category of deep-seated gravitational slope deformation (DSGSD) generally includes double ridges/sagging phenomena. Some very typical features have been recognized along the valley sides and the upper plateau areas around VM and in particular of Tithonium and Candor Chasma, Melas Labes, Geryon Montes, and Coprates Labes (Figure 9). These phenomena resemble those recognized in mountainous areas on the Earth and described as sagging or deep-seated gravitational slope deformations (Crosta, Frattini, & Agliardi, 2013). We prefer in this case the first definition because the mapped features are not often associated to a clear slope deformation (e.g., laterally defined limit for the scar and crown areas, toe bulging) both in plane and cross view. Mège and Bourgeois (2011) suggest the presence of these gravitational features along VM. However, except for Geryon Montes in Ius Chasma where the double crest likely indicates a form of gravitational splitting (Figure 9c), some of these forms are dubious because they might be associated with the typical trenches observed along the upper plateau beyond the valley crests. In fact, their extraordinary length (hundreds of kilometers) associated with constant geometrical characteristics would rather suggest a structural origin (faults or major master joints) put in evidence by erosion. Locally, large slumps developed along some of these features. This could suggest again a structural control and their passive control on the development of large slumps and rock avalanches (e.g., Coprates Labes and Ius Chasma).

4. Statistical Analysis

4.1. General

The robustness of the landslide inventory allows to extract information about the general characteristics of the landslides, their distribution, and the morphological characteristics of both the landslides and of the landscape where they occurred.

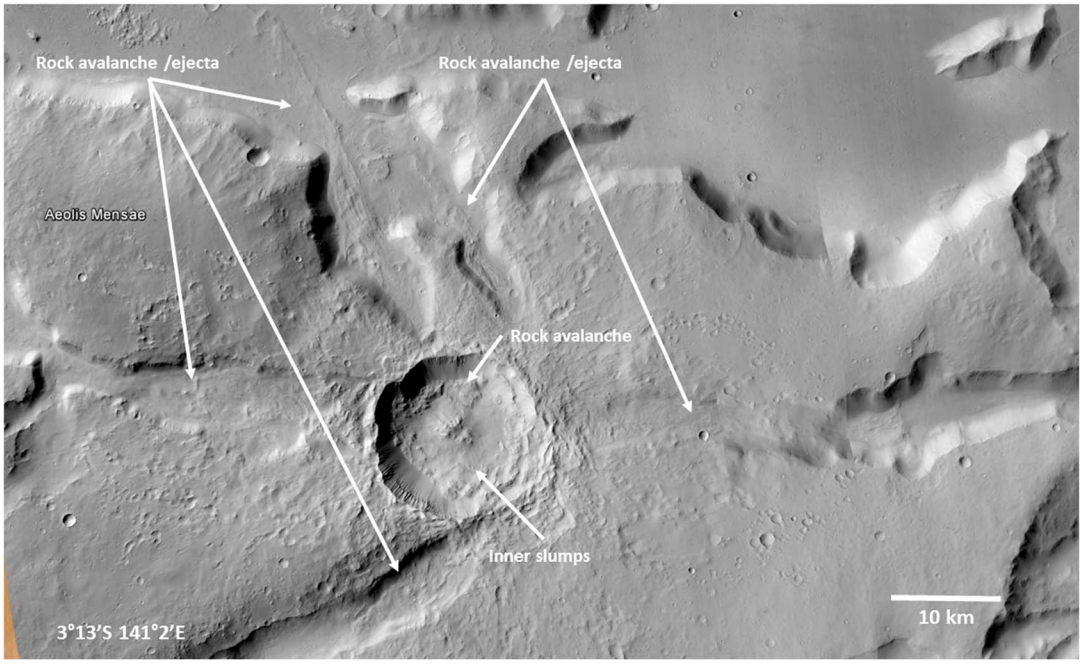

Figure 8. Examples of rock avalanche/ejecta deposits in the Aerolis Mensae region, characterized by long flow tongues outside the crater rim and by flow-like features developing within incised valleys radially developed from the crater rim. Inner slumps and a rock avalanche are shown.

4.2. Geographical Position

Martian landslides are widespread across the entire planet. Figure 10 shows that rock avalanches dominate in most of the areas except Xanthe and Margaritifer Terrae and at the outflow channels (Shalbatana, Kasei) and the volcanoes of Alba and Elysium Montes where slump/flows are more numerous. The maximum concentration of landslides is observed along the main valley system of Mars, extending along the west-east axis from Noctis Labyrinthus to Margaritifer Terra. Rock avalanches are dominant in VM and widespread across the entire planet (Figure 10a), with high concentration in Tyrrhena Terra and Terra Cimmeria. In terms of size,

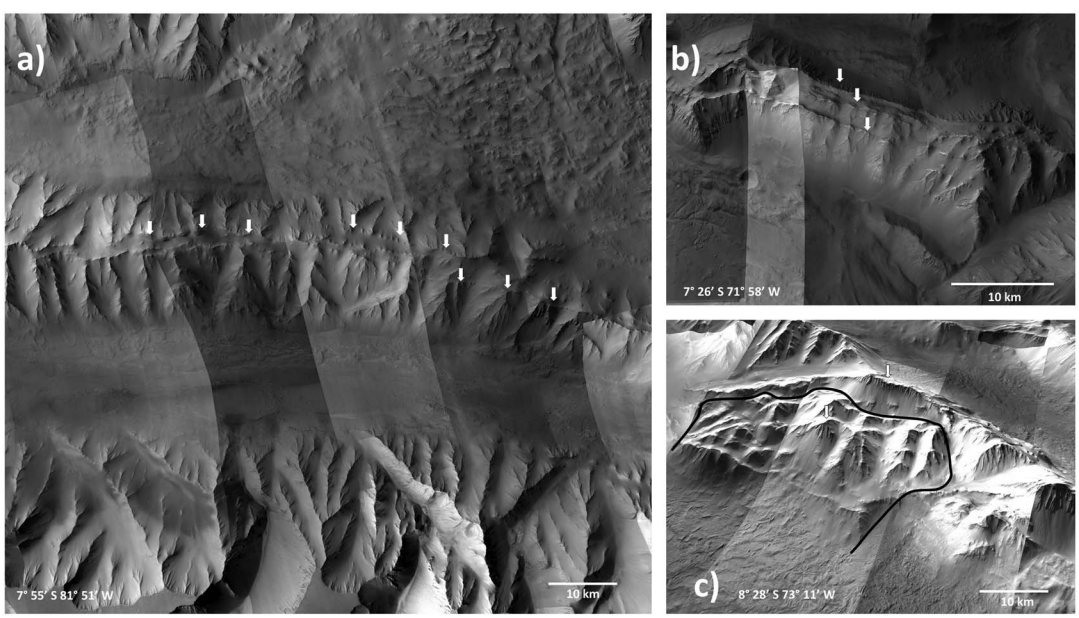

Figure 9. Examples of sagging/deep seated gravitational slope deformations: (a) long double ridge developing parallel to the main valley axis with no clear deformation of the slope toe; (b) multiple ridges with possible scarps and counterscarps association; (c) large slumped blocks separated by persistent subparallel linear features with an oversteepened toe sector.

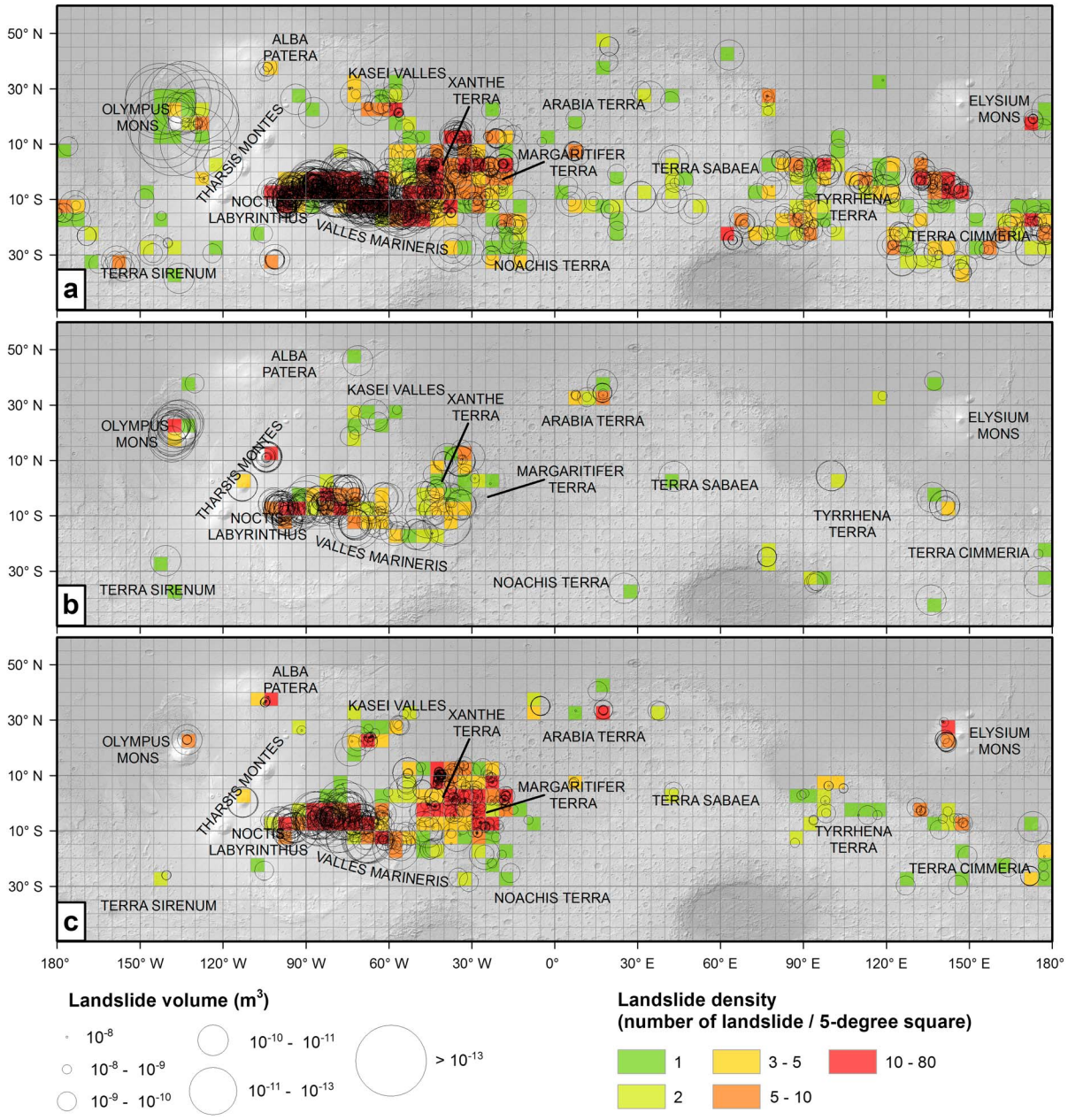

Figure 10. Map of the distribution of rock avalanches (a), slumps (b), and slump/flow (c) at the planet scale as from this study. Landslide volumes are computed based on the empirical relationships obtained by reconstruction of the failure surface (section 2.3) for a set of 222 landslides (Figure 1b). Landslide density is calculated as number of landslides per 5° squares.

the Olympus Mons aureoles are by far the largest landslides in whole Mars, followed by those in the central sector of VM. Slumps occurring in craters have not been mapped systematically due to the huge number and their physical direct association to most of the impact craters. The spatial distribution of slumps shows a maximum concentration in Noctis Labyrinthus and VM (Figure 10b) with the largest slumps around Olympus Mons and in the central and eastern parts of VM. Large slumps/flows are mostly located in VM (Figure 10c), while small slumps/flows are present in Margaritifer Terra in other areas of Mars, with hot spots in Alba Patera, Kasei Valles, and Elysium Mons.

Landslides on Mars tend to cluster within a narrow latitude range. Most of landslides lie between 15°S to 15°N. This is partially related to the distribution of local relief on Mars, calculated from the MOLA DEM using a circular moving window with a radius of 5 km. For latitude higher than 30°, landslides almost disappear

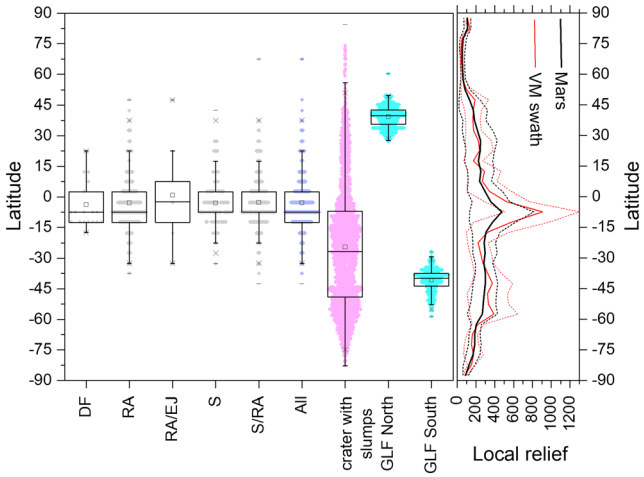

Figure 11. Distribution of landslide types (DF: debris flows; RA: rock avalanches; RA_EJ: rock avalanches/ejecta; S: slump; S-RA: slump-rock avalanche) according to the latitude. The highest density is always in the equatorial areas. The distribution in terms of maximum latitude is well represented with very few landslides occurring beyond 30°S and 22°N, 5 km. Local relief is represented in the side plot. Black line is the relief over the entire planet, while red line is the relief for the latitude range of Noctis Labyrinthus-VM-Margaritifer Terra zone (110°S–5°S). Dashed lines represent ±1 standard deviation of mean local relief.

(Figure 11). In the northern hemisphere, this is due to a flattening of the Martian topography. In the southern hemisphere, local relief does not change much up to 60°S, as also testified by the high number of slumps in craters (Robbins & Hynek, 2012; Figure 11).

4.3. Slope Angle: Stable Versus Unstable Slopes

Slope instability increases with relief and slope angle. To verify to what extent the steepest slopes are associated to high landslide density, we studied the local slope angle for different regions of Mars in near proximity of the mapped landslide scarps, excluding the flat areas at the slope toe and beyond the crest (e.g., VM upper plateau; Figure 12a). The slope angle progressively increases when moving toward the equator with maximum values in the VM-Noctis Labyrinthus equatorial region between −5°S and −20°S (Figure 12b). In the northern hemisphere, high slope angles are observed in Margaritifer Terra, Kasei valley, Alba Patera, and Elysium Mons. With the exception for these areas, slopes to the north and south of the VM area show lower inclination. In this analysis, we may keep in mind that slope angles are underestimated, being derived from low-resolution DEMS.

In Figure 13 we show the distribution of unfailed and failed slopes in VM (Crosta et al., 2014) in a two-dimensional plot where the abscissa represents the slope angle and the ordinate scale the hillslope relief. Instability increases toward the right-hand side and high portion of the plot. According to the upper-bound limit-analysis approach for slope stability (Utili & Crosta, 2011), the critical conditions between stable and unstable slopes are represented by the three lines obtained by assuming different rock mass properties (i.e., cohesion and friction angle; Crosta et al., 2014). Note that unfailed slopes are below the instability line. The landslides of the inventory, for which we calculated the slope angle of the main scarp, are even lower, indicating that slope failure has resulted in more stable slope.

4.4. Deposit Geometry and Morphology

The deposit geometry can be indicative of the modes of deposition, the type and properties of the materials, the landslide velocity and its distribution, and the constraining effect of other topographic features. In this

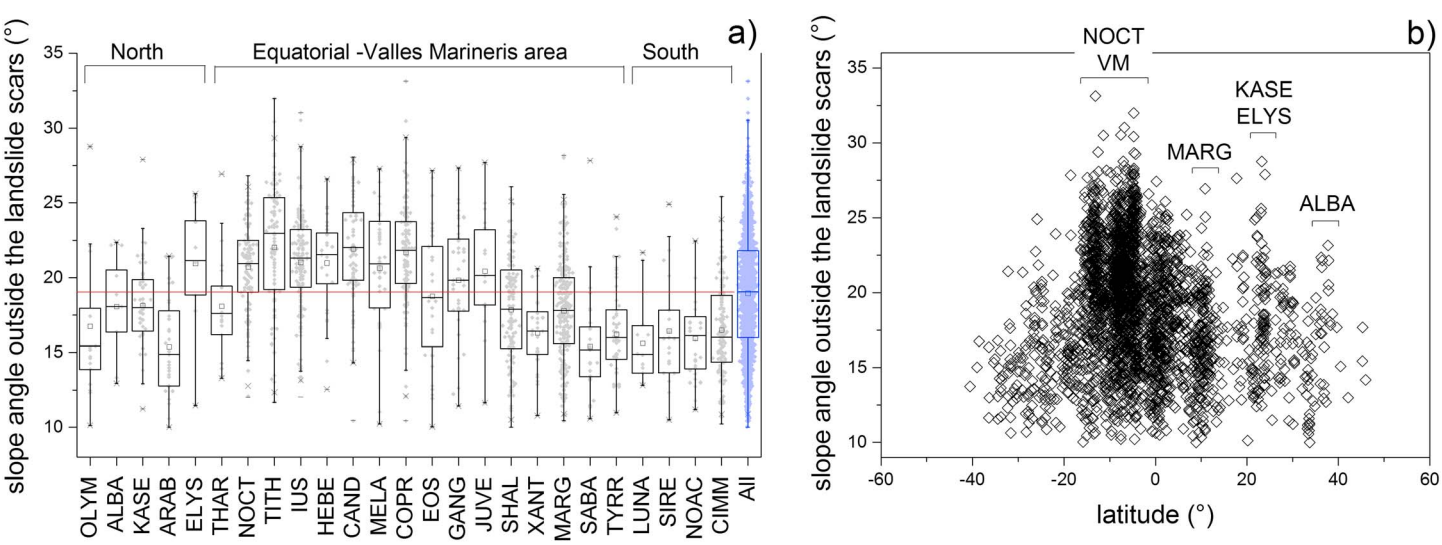

Figure 12. Slope angle outside the landslide scar within a buffer of 500 m. (a) Box plots are grouped on the basis of the region location: northern and southern hemisphere high latitudes, equatorial regions. Within each macro zone, the regions are reported moving from W to the E. Labels are as in section 2.2. The red line corresponds to the median value of the whole landslide population. (b) Slope angle outside the landslide scar as a function of latitude. Local peaks are labeled.

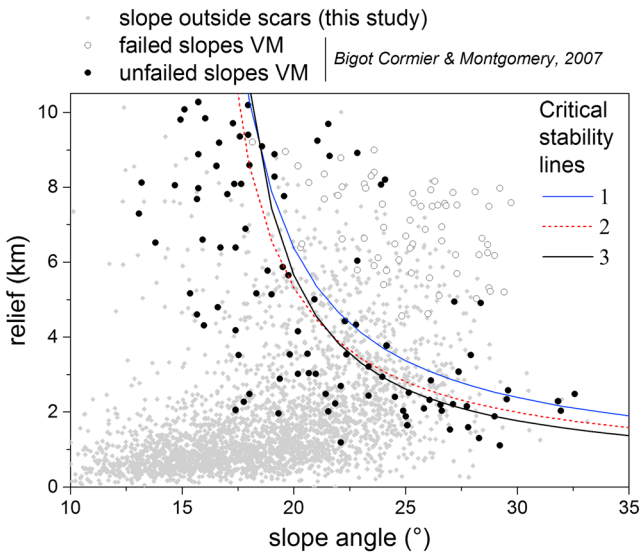

Figure 13. Plot of local relief versus slope angle for slopes affected and unaffected by landslides. The slope angles of the main scarp of the landslides (gray point) fall below the critical lines. Critical stability lines are computed from upper-bound limit-analysis (Crosta, Frattini, & Valbuzzi, 2013): line 1: $\varphi = 14°$, $c_1 = 1.5$ MPa, $c_2 = 2.9$ MPa; line 2: $\varphi = 14°$, $c_1 = 1.25$ MPa, $c_2 = 2.65$ MPa; line 3: $\varphi = 15°$, $c_1 = 1.0$ MPa, $c_2 = 2.4$ MPa.

study, the area (A_d), length (L_d), and width (W_d) of the deposits have been examined for each landslide. The deposit area and the L_d/W_d ratio show the highest values in the southern hemisphere between −5°S and −15°S (Figure 14). Secondary peaks occur at 10°N, 22°N, and 30°S (see labels in Figures 14b and 15).

The median L_d/W_d ratio on Mars is 1.25, with higher values in VM, especially in Juventae Chasma, and in the craters of Terra Sabaea, Tyrrhena Terra, Terra Cimmeria, and Noachis Terra.

Figure 16a is a scatterplot of the scar area, A_s (i.e., the area of the failure surface exposed by the landslide movement), with respect to the deposit area, A_d. Due to the combined effect of thinning of the deposit and of volume bulking associated to the landslide motion and rock fragmentation, the deposit area is larger than the scar area. The same behavior is confirmed when comparing the deposit area with the failure area, A_f (total area of the reconstructed failure surface), that has been reconstructed for a selected subset of 222 landslides (Figure 16a). This plot allows also to interpret data in terms of the change in thickness of the landslide passing from the source to the final deposit and so to the mean stress acting along the failure surface and the basal surface during spreading.

Distinguishing among the different typologies reveals some trends (Figure 16b). Values below the median (horizontal line in Figure 16b) are associated to deposits closer to scar areas (compared to other typologies) occurring for thick slumps (S) or for those phenomena where part of the deposit remains over the failure surface. This condition occurs for slumps and slump/flows, characterized by a steep and narrow portion of the main scarp and another flatter portion engulfed by landslide material. Debris flows are in general characterized by relatively short deposits with respect to long source and transportation areas, resulting in low A_d/A_s values. In contrast, rock avalanche-ejecta (RA_EJ) are found to be higher than median. This is a consequence of the strong energy involved in the initial horizontal propagation of the ejecta, resulting in the complete emptying of the source zone and a relatively long transportation zone.

4.5. Emptying of Scar Area

The degree of preservation of Martian landslides allows us to determine the fraction of material that has emptied the scar area. This has never been analyzed in detail, but it can be extremely helpful in supporting theories concerning the type of material or the mechanisms controlling the strength loss along the failure surface. It is observed that in many cases, the deposit rests within the scar area, whereas in other cases it

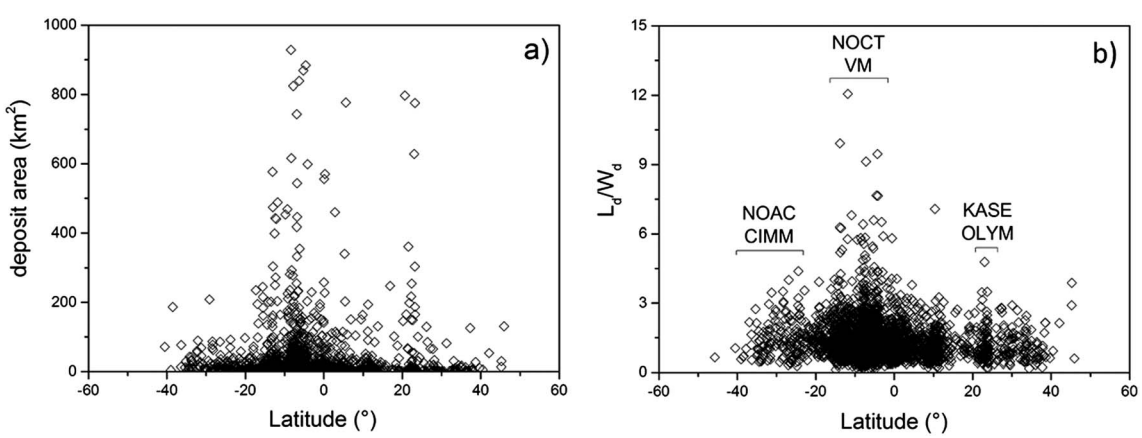

Figure 14. Geometrical characteristics of deposits as a function of latitude: (a) area, (b) length to width ratio, L_d/W_d. The geographical reference for the most evident peaks is shown by labels as in section 2.2.

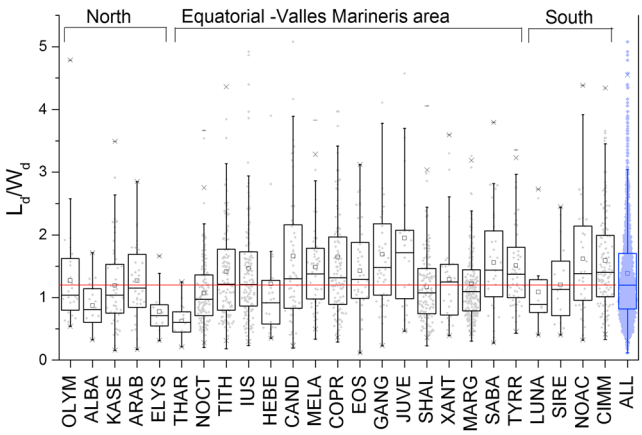

Figure 15. Length (L_d) to width (W_d) ratio for the landslide deposits represented for different Martian regions. Box plots are grouped based on the geographical location: northern and southern hemisphere high latitudes, equatorial regions. Within each macro-zone, the regions are reported moving from W to E. Labels are as in section 2.2. The red line corresponds to the median value of the whole landslide population.

completely abandoned the scar. Starting from the 222 reconstructed landslides, Figure 17 shows the scar area left uncovered by the landslide as a function of the total failure surface area. A 1:1 relationship (black solid line) indicates a condition in which the failure zone has been completely evacuated by the material (i.e., scar emptying of 100%). Note that the ratio between scar area and failure surface area tends to decrease with increasing the landslide volume (colors in Figure 17). Thus, while a small landslide typically leaves the source area, a large one tends to remain partially within its own scar, probably due to low slope associated to larger landslides. Furthermore, larger landslides are usually characterized by deep-seated failure surfaces with steep upper scarp sectors associated to tension cracks and with decreasing slope angle of the failure zone in the toe region. All this results in the deposition of the material in these lower sectors.

4.6. Runup: Relationships With Topography and Materials Covering the Spreading Path

The observation of relationships between the landslide deposit and the topographic surface, inclusive of information about the materials forming this surface, is relevant for the understanding of landslide mechanics during the runout phase. We mapped several features originated by the interaction of the moving mass with the ground surface, such as the formation and deviation of lobes within the moving front because of topographic obstacles (e.g., small mounds and ridges, valley flanks, crater rims, and other landslide deposits), and the presence of material scraped or bulldozed by the landslide, from the original ground surface over which spreading occurred (see supporting information Figures S9 to S11). Channeled phenomena with evident final depositional lobes on the open flat plains, and sometimes lateral levees within the channel, have been mapped. The runup of the landslide front is evident at various sites in VM and outflow channels, where the opposite valley side is often within reach of the front of largest landslides. The runup is often appreciated on the images, and the difference in topographic height may allow computation of landslide velocity. Likewise, mounds and ridges protruding from the landslide path provide a means of estimating the landslide thickness and velocity at these locations.

Figure 18 shows the runups reached by the landslide fronts, R, normalized by the drop height, H (i.e., difference in elevation between the crown area and the deposit extreme tip), for different confinement conditions (Figure 18a) and environmental settings (Figure 18b). Runup occurs only with a frontal confinement (F and BF

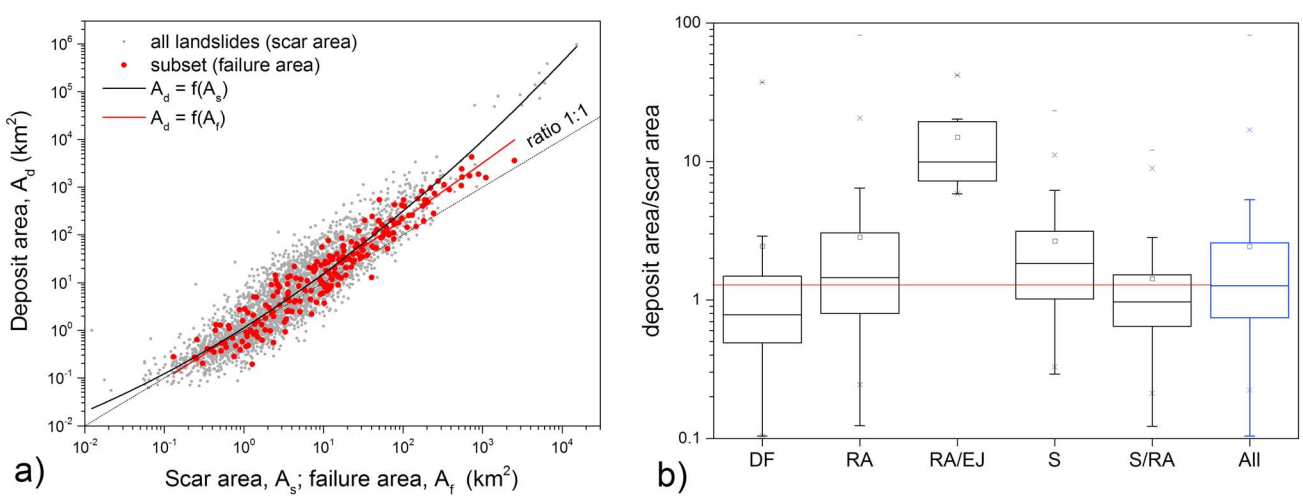

Figure 16. (a) Scar versus deposit area for all the mapped landslides (black fitting line: $\log A_d = 2.825 + 0.026 \log A_s + 0.085 \log A_s^2$, Adj $R^2 = 0.84$). For a selected subset (222 reconstructed landslides, red dots), the failure area is plotted against the deposit area (red fitting line: $\log A_d = 0.014 + 0.91 \log A_f + 0.016 \log A_f^2$, Adj $R^2 = 0.91$). (b) Box plots of the deposit to scar area ratio for different landslide types. The plot implicitly represents the change in landslide depth at the source and in the deposit and then the characteristics of the material forming the deposits. The red line corresponds to the median value of the whole landslide population.

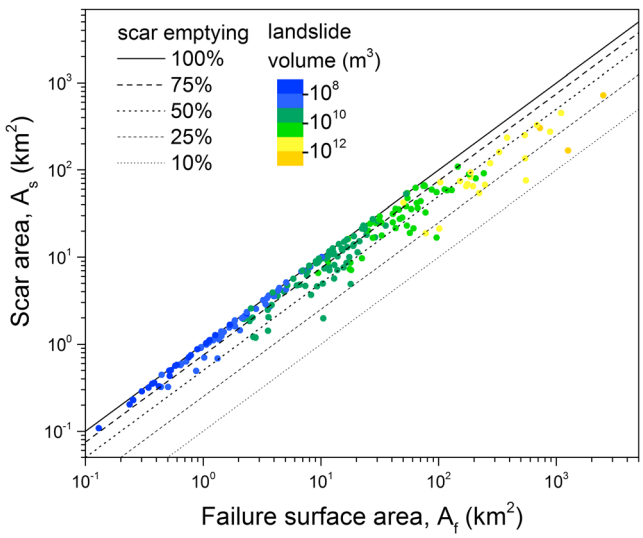

Figure 17. Scar versus failure surface area for a selected subset of 222 landslides reclassified as a function of landslide volume. Lines representing different values of scar emptying, from 100% to 10%, are drawn showing a decreasing emptying with increasing landslide volume.

in Figure 18a). The reflection of landslide front (RR) occurs only with an *R*/*H* ratio exceeding 0.1, indicating a runup larger than 10% of the total drop height. The largest runup occurs for landslides located outside of impact crater rims (AOC) and for landslides within labyrinth (L) and secondary valleys (SV; Figure 18b). The first condition (AOC) is associated to extremely high mobility associated to the extra energy contribution and the material properties (i.e., following the impact), while the second condition (L and SV) may reflect a higher frontal confinement.

4.7. Magnitude-Frequency Relationships

The frequency distribution of landslide size may reveal important information related to the landscape morphology (Frattini & Crosta, 2013; Ten Brink et al., 2009), the geological structures (Katz & Aharonov, 2006), and the materials (Frattini & Crosta, 2013; Katz & Aharonov, 2006; Stark & Guzzetti, 2009) affected by the landsliding. The literature on landslide size distribution shows that the frequency distribution normally exhibits power law scaling for landslides larger than a size threshold and that, below this threshold, the distribution shows a deflection and deviates from power law. In some cases, the deflection occurs right below the modal peak of the distribution, known as rollover (Frattini & Crosta, 2013; Malamud et al., 2004).

We developed noncumulative log-binned magnitude frequency relationships, from which we calculated a probability density, *p*, as a function of landslide area, *A* (Figure 19). For the entire Martian inventory, we observe a scaling exponent $\beta = 1.02$ for 10^6 m$^2 < A < 3 \times 10^7$ m^2 and $\beta = 1.55$ for landslides larger than 3×10^7 m^2. Among the confined landslides, we observe a lower exponent, thus suggesting a prevalence of larger landslides with respect to the entire data set. In the different geomorphological settings, the scaling exponent varies from 1.17 to 2.11. Lower exponent associated to larger landslides can be found in volcanic areas (here, the Olympus Mons areolae control the scaling exponent; OV in Figure 19) and main valleys (MV). Higher exponent associated to a prevalence of relatively smaller landslides characterize secondary valleys (SV) and landslides associated to craters (IC, AOC, and AIC; see Figure S15).

A complete set of plots with magnitude-frequency curves for landslides mapped in different areas is presented in the supporting information.

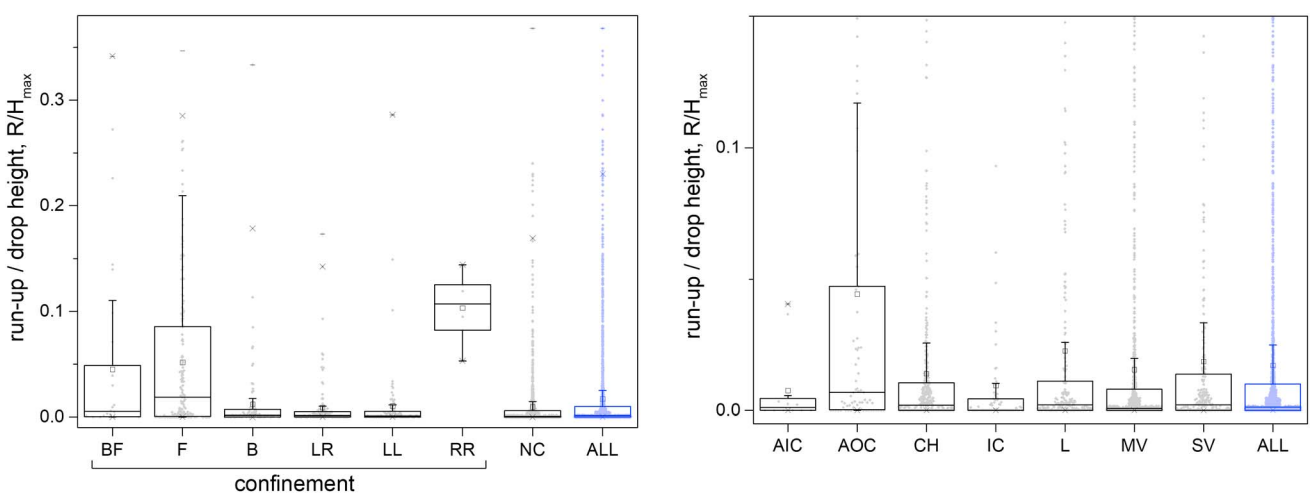

Figure 18. Box plots of runup to drop height ratio for different confinement conditions (a) and different geomorphological settings (b). Labels are as in section 2.2 (see the supporting information for detailed description).

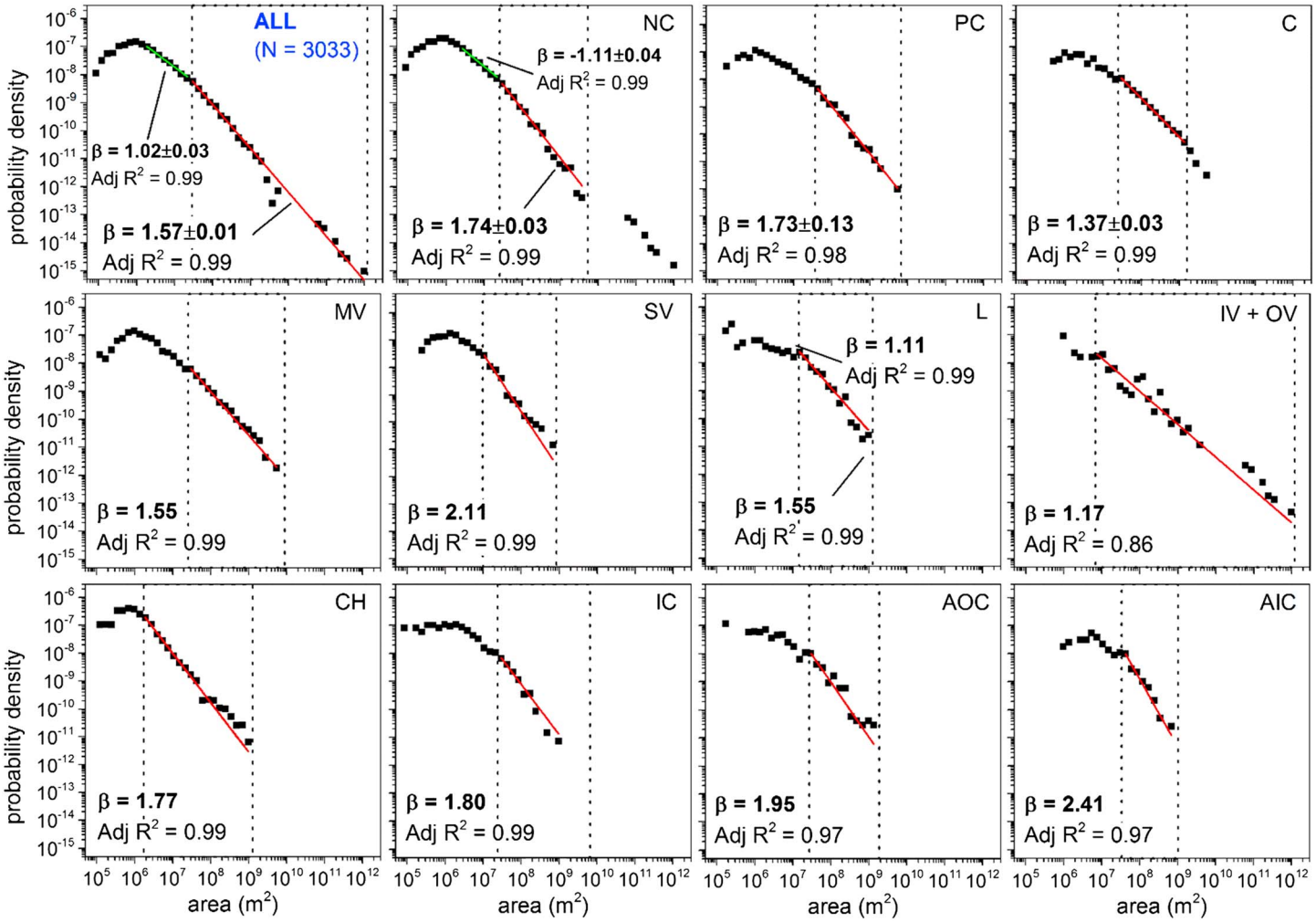

Figure 19. Noncumulative log-binned magnitude frequency relationships for Martian landslides with different degree of topographical confinement: unconfined, NC; poorly confined, PC; and confined, C, and in different geomorphological settings. Labels are as in section 2.2. The power law scaling exponent is reported together with the Adjusted R^2 of the fit.

4.8. Landslide Volume

Various authors proposed relationships for the estimate of landslide volume starting from the landslide area (Larsen, Montgomery, & Korup, 2010; McEwen, 1989). Most of these relationships do not introduce any clear distinction or subdivision for the total landslide area (i.e., inclusive of scar, transportation, and deposition areas), and the volume relationship is often derived from a relatively limited data set of landslides without estimating the associated error.

As detailed in the section 2, pre-event and postevent topography and failure surface have been reconstructed for 222 landslides, from which we obtained both the failed volume and the deposit volume. By using these volume estimates, we tested different relationships with the area of deposit, the area of the scar, and the total area. The best fitting relationships have been obtained between (a) the volume of the deposit, V_d, and the area of the deposit; (b) the mean volume, V_{mean} (i.e., the average of deposit and failed volumes) and the area of the deposit; and (c) the mean volume and the total landslide area (Figure 20). Among these relationships, we believe that the second is the most reliable. In fact, the use of the deposit volume (Figure 20a) brings large uncertainties for smaller landslides with relatively shallow deposits, while the total area (Figure 20c) is not meaningful for landslides with a large emptying of the scar. For the mean volume-deposit area relationship, we applied bootstrapping to assess the uncertainty of the power law exponent (Figure 20b). The exponent ranges between 1.12 and 1.24 for Martian landslides, to be compared with an exponent 1.39

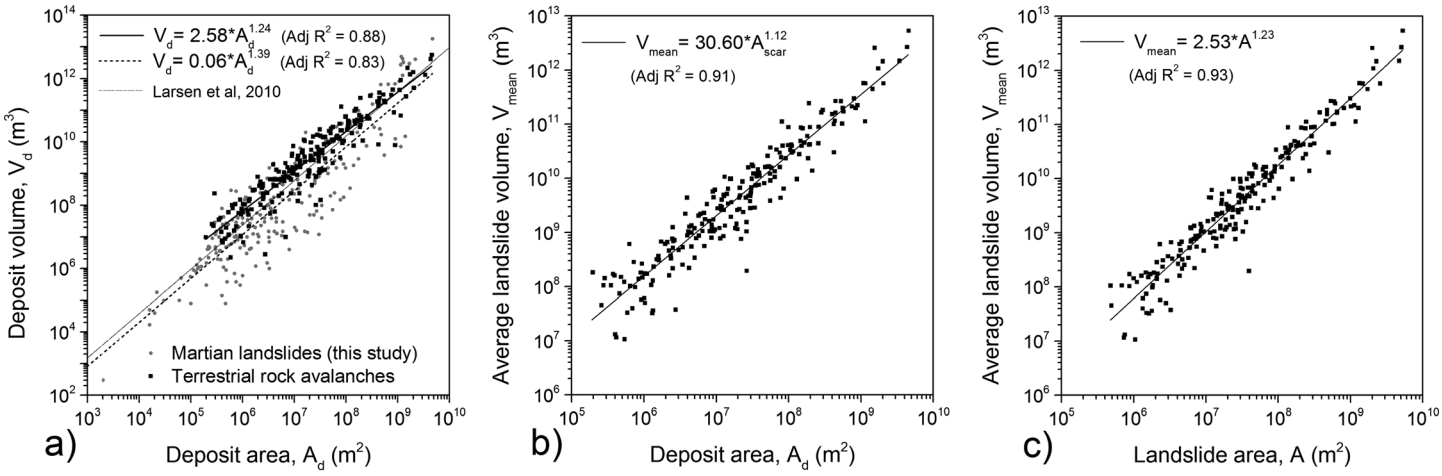

Figure 20. Series of plots for volume to area data. (a) Landslide deposit volume versus deposit area relationships for 222 Martian and 226 terrestrial landslides (Capra et al., 2002; Larsen et al., 2010; Legros, 2002; Sosio, Crosta, Chen, et al., 2012; and references therein). (b) Average landslide volume versus deposit area for Martian landslides; (c) average landslide volume versus total landslide area. Average volume is computed by averaging the values for the reconstructed niche volume and the deposit volume. The total area is the sum of the scar and deposit areas. Martian landslides are less mobile than terrestrial phenomena with a decrease in difference for larger phenomena.

for terrestrial landslides. It is worth to notice that the two data sets for terrestrial and Martian landslides are of similar size (approximately 200 events).

4.9. Landslide Mobility

While mapping the landslides as polygons, the maximum length and breadth of each landslide deposit have been mapped. These, together with the maximum loss in elevation (or drop height, i.e., difference in elevation between the crown area and the deposit extreme tip), allow drawing some conclusions about the landslide mobility and the size of the deposit. The *H*/*L* ratio is widely used in the literature for this aim, and it is regarded in the literature as a proxy for the dynamic friction angle of the landslide: the lower the *H*/*L*, the higher the mobility of the landslide. Over the Mars planet, the *H*/*L* ratio shows a clear dependence on landslide volume (Figure 21), with larger mobility associated to larger landslides. As expected, rock avalanches are more mobile than slumps and slump/flows. However, the mobility seems controlled by the geographical and geomorphological setting. In fact, it appears to be lower for landslides in the equatorial areas, and especially in VM (Figure 21a). On the other hand, mobility tends to increase toward the high latitudes, especially in the southern hemisphere (Figure 21b).

Regarding the geomorphological settings (Figure 21c), it clearly appears that mobility is relatively low in main and secondary valleys (MV and SV, respectively), in Noctis Labyrinthus (L), and along volcano flanks (IV and OV). Landslides in the Labyrinthus are more mobile than those in the main valleys suggesting the possible presence of some controlling factor either physical or mechanical. On the other hand, landslides associated with craters (AIC, AOC, and IC) result more mobile and well below the mean *H*/*L* value calculated for the entire landslide population. Data dispersion is generally larger for landslides occurring in chaos, volcanoes, and main valley system.

5. Discussion

5.1. General Assessment

The present landslide inventory, which provides data for 3,118 landslides, is an important step in the understanding of the Martian environment and its changes through time. As shown in Figure 1, the number of landslides mapped in the sole VM region, from Noctis Labyrinthus to Coprates Chasma, amounts to about 1,200. This is a very large data set if compared to those already existing in the literature for the same area (Brunetti et al., 2014; Crosta, Frattini, & Valbuzzi, 2013; Lucchitta, 1979; Quantin, Allemand, & Delacourt, 2004; Shaller, 1991). At the same time, the completion of this inventory allowed to verify some of the previously mapped features and to discard some of them because they are not considered representative of a

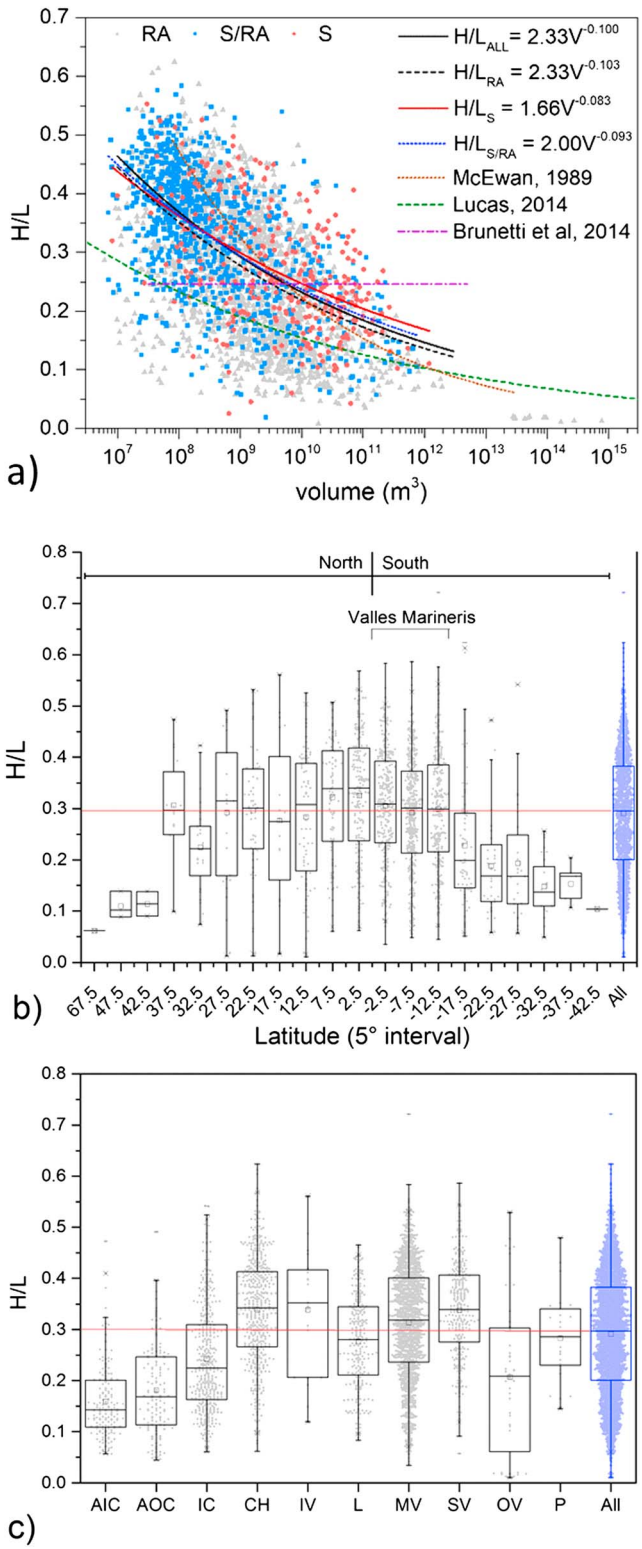

Figure 21. (a) *H/L* ratio as a function of volume for different landslide typologies; (b, c) box plots of the drop height to length ratio distribution for (b) latitude and (c) geomorphological setting. The red lines correspond to the median value of the whole landslide population. Labels are as in section 2.2 and in the supporting information.

landslide or because of their glacial and periglacial nature. In this way, a robust analysis has been presented also beyond the most obvious regions of landslides on Mars, viz., VM and the system of equatorial vallis, labyrinthus, and chaos. In fact, partial studies covering only portions of VM cannot support an analysis at the global scale. For example, 83 landslides (generically described as slides in Brunetti et al., 2014) cannot provide a robust data set for *H/L* ratio determination in environmentally variable conditions, such as those typical of Martian vallis, when considering the dependency of this ratio on landslide volume (see Crosta et al., 2018) and local conditions. Furthermore, no analysis has been previously performed on the landslide distribution with latitude and on the different geometrical (e.g., length to width ratio) features characterizing the source and the deposit areas. In this study, the volume versus area relationships proposed in the literature (Larsen et al., 2010; Legros, 2002; McEwen, 1989) have been tested, and a clear difference is put in evidence. In the following, the main results are discussed with respect to the existing knowledge concerning both Martian landslides and their terrestrial analogues.

In the present database, the relationships of landslides with regard to chronology have not been explored. Due to the extreme labor associated with surface dating on Mars, only an insufficient number of landslides have been dated in previous publications (Grindrod & Warner, 2014; Hager & Schedl, 2017; Quantin, Allemand, Mangold, et al., 2004), and thus, drawing general conclusions as to landslide distribution and typology as a function of the ages is not possible. A second important point that has not been considered is the relationship between landslide properties and the geology of the terrain, as detailed in the geological map of Mars (Tanaka et al., 2014).

5.2. Landslide Distribution

Most of the landslides are concentrated (Figures 1, 10, 11, and 12) along the equatorial vallis and chaos system, the northern Kasei Valles, Margaritifer Terra, and the Martian Dichotomy. At the planet scale, landslides cover a latitude interval between 30°S and about 22°N with very few occurring beyond such limits. No significant landslides have been found at latitudes higher than 40°S and 46°N. Simple slope stability methods applied to the Martian terrain such as the Culmann's model (Bigot-Cormier & Montgomery, 2007) as well as more advanced limit analysis and numerical models (Crosta, Utili, et al., 2013; Schultz, 2002) show that, not differently from Earth, instability requires both a steep and high relief. The distribution of Martian landslides found in our database reflects such conditions, the excluded areas lacking the relief necessary for landslides to occur. In particular, the 20°–30° steep slopes in 5,000–9,000 m high VM explain the high concentration of landslides along these equatorial valleys. Landslides to the north and south of the VM area are characterized by lower inclination and relief (Figure 13). This indicates that failures have occurred because of weaker rocks and/or the .abundance of water or ice, suggesting the presence of different environmental conditions.

In addition to the relief, we find a complementary distribution associated to glacial and periglacial features as mapped by Souness

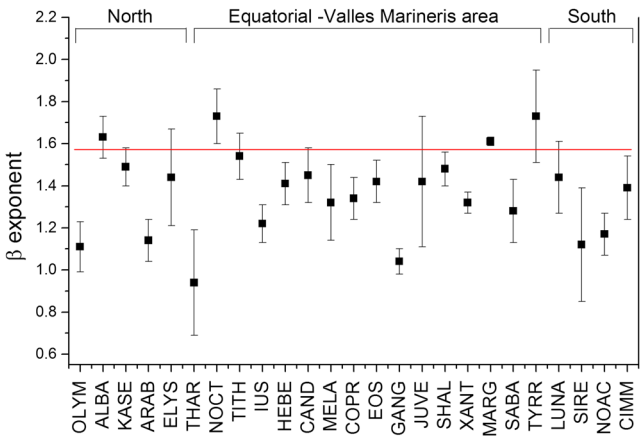

Figure 22. Power law scaling exponent, β, of noncumulative log-binned magnitude frequency relationships for different regions. See Figure S12 for all the magnitude frequency curves (supporting information). Whiskers represent the standard error of the exponent estimation. The red line corresponds to exponent of the whole landslide population.

et al. (2012; see Figures 1 and 13). This is possibly related to the lower temperatures and the abundance of ice favoring the occurrence of periglacial and glacial processes. Therefore, such processes control the dismantling of the Martian slopes at higher latitudes. At the same time, large landslide-like deposits could still be found but characterized by much smoother surfaces, with less sharp longitudinal and convoluted ridges and furrows. These forms could be due to periglacial and glacial processes reworking old landslide deposits. The reduced number of impact craters affecting these deposits (Hartmann & Werner, 2010) suggests the degree of activity or the more recent activity of such forms with respect to landslides. Therefore, they also suggest that landslide deposits and features could have been strongly reworked and masked by glacial and periglacial processes.

Slumps associated with impact craters have not been mapped in this study, but their presence is reported in the impact crater database by Robbins and Hynek (2012) for craters with diameter larger than 1 km. These authors simply indicate the presence but do not map the features. These slumps, common to other planets and moons and sometimes erroneously defined rockslides, appear almost homogeneously distributed over the Martian surface (see Figure 11). In fact, they are directly associated to the crater formation or to the destabilization of the crater slopes because of the rock mass properties degraded by meteoroid impact.

5.3. Magnitude Frequency Relationships

As described in section 4, the power law scaling is characterized by a bilinear trend with a scaling exponent of $\beta = 1.55$ for areas larger than 3×10^7 m^2, a deflection of the frequency ($\beta = 1.02$) for 10^6 m$^2 < A < 3 \times 10^7$ m^2, and a marked rollover below a size of 3×10^7 m^2. These values update preliminary ones (Crosta, Frattini, & Valbuzzi, 2013) based on a much smaller data set in which the power law scaling was $\beta = 1.11$ for smaller landslides and $\beta = 2.19$ for the largest ones. A power law scaling exponent $\beta = 1.35$ was found by Brunetti et al. (2014) for all landslide types. The deflection observed below 3×10^7 m^2 witnesses an undersampling of smaller landslides, typical for nonevent inventories (Malamud et al., 2004), due to either the resolution of the imagery used for the interpretation or the censoring of small landslides masked by postlandslide deposits. On Mars, such postlandslide draping may be due to ancient water and ice-associated deposits or modern Aeolian deposition, similar to the resurfacing affecting crater counting at low crater diameters (Platz et al., 2013). The abrupt rollover below 3×10^7 m^2 together with undersampling is suggestive of a physical control, probably due to the role of stress- and size-independent cohesion on the shear strength (Frattini & Crosta, 2013). Interestingly, the rollover occurs at a value much larger compared to Earth (Frattini & Crosta, 2013; Malamud et al., 2004), although the resolution of imagery is comparable for most terrestrial inventories. This could be associated to the smaller gravity of Mars, which force landslides to be larger to overcome the rock resistance (especially cohesion), which is comparable to terrestrial values.

Comparing the scaling exponent of landslides with different degree of geomorphological confinement (unconfined, NC, poorly confined, PC, and confined, C, see Figure 22), we observe a decrease of the exponent with increasing confinement. This suggests that, for confined conditions, the proportion of larger landslides is higher with respect to unconfined conditions, which is apparently counterintuitive. However, this result reflects the fact that we classified as "confined" landslides that reach with their front (or laterally) other landslides or the opposite valley or a crater slope. This condition is normally satisfied by larger landslides, thus justifying the gentler scaling exponent. At the same time, the topographical constraining effect on Mars seems to be poorly effective on the landslide runout (and area) with respect to the terrestrial counterparts, this being witnessed by numerous landslides with significant runup, as will be further discussed.

Comparing the scaling exponent for landslides occurring in different regions (Figure 22), significant differences become evident. The exponent is smaller for landslides associated to volcanic edifices (OLYM, THARS). Here landslides tend to be proportionally larger, probably linked to the effect of the huge

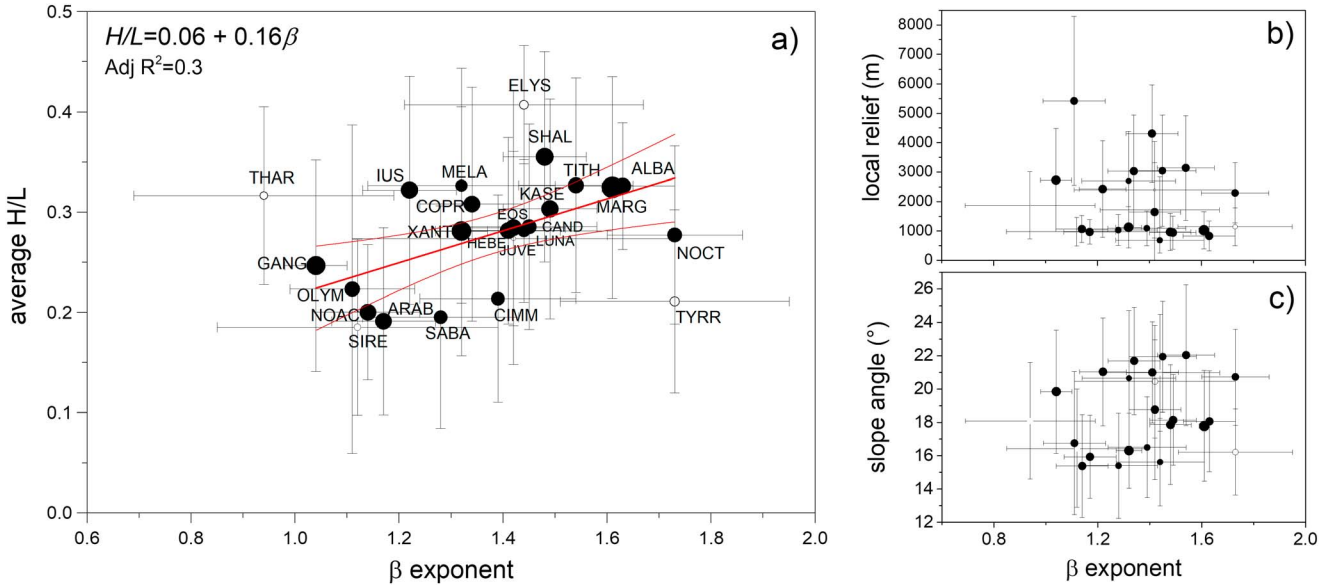

Figure 23. Average *H/L* ratio (a), local relief (b), and slope angle outside the scar (c) as a function of the power law scaling exponent, β, for different regions. The fitting line and the 95% confidence bands are calculated only for points with a standard error lower than 0.2 (black circles). Whisker length represents the standard error of the exponent estimation and the standard deviation of *H/L*, local relief, and slope angle. The symbol size (open and black circles) is inversely proportional to the standard error of the exponent estimation.

landslides around the Olympus Mons volcano. On the other side, the exponent is larger for Noctis Labyrinthus and Margaritifer Terra, suggesting a prevalence of relatively small landslides (see also Figure 19).

We found that the scaling exponent is positively correlated with the landslide mobility: the larger the mobility (low *H/L* ratio), the lower the value of the scaling exponent (Figure 23a). This is a novel way to interpret the scaling exponent value, and the observed behavior can be partially explained as an indirect effect of landslide volume. In fact, the mobility is higher in regions where larger landslides dominate over smaller ones, which in turn causes the power law exponent to be low. This can also explain the slight dependence of the exponent to local relief (Figure 23b), since a larger local relief can result in larger landslides, giving a lower exponent. However, the exponent shows also a negative correlation with slope angle outside the scar (Figure 23c). Both experimental and real scale observations suggest that a decrease in mobility occurs at increasing slope angle (Crosta et al., 2015). On the other hand, slope angle is not correlated with landslide volume as it may happen for *H/L* ratio or the local relief. This suggests that the exponent β may be actually controlled by landslide mobility. Since the area of landslide used to calculate the frequency-magnitude relationship also includes the deposit, we can explain the control of mobility with the tendency of high-mobile landslide to spread over, thus resulting in larger accumulation areas with respect to the landslides with the same volume in areas where mobility is reduced.

5.4. Landslide Geometry and Volume

Martian landslides are characterized by variable geometries even when occurring in very similar environments. Mapped failure surfaces and scars can be hemispherical, elongated, box shaped, stepped, or terraced. In turn, these characteristic geometries can affect the final deposit geometry and material distribution. The deposit geometry, in terms of length to width ratio, shows that landslides in the VM system are generally more elongated. This may be due to dynamical reasons (for example, increase of basal lubrication), to topographic controls (e.g., valley bottom inclination and degree of confinement) or to material properties (e.g., presence of finer material and increasing ice and water content). This is in agreement with the finding that up to a certain slope value, the horizontal velocity component (i.e., parallel to the local geoid) is dominant. At steeper slopes, the vertical component becomes progressively dominant causing an increase in the lateral spreading of the material (Crosta et al., 2015). This supports the hypothesis that high relief slopes can cause high longitudinal velocity components. More equidimensional deposits are typical of northern and southern regions where the presence of ice is more abundant and could have controlled the post-depositional

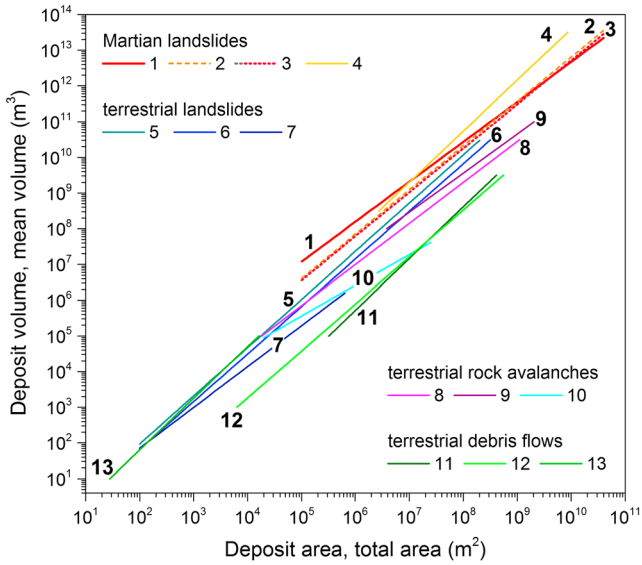

Figure 24. Volume versus area relationships for Martian and terrestrial landslides, $V = \alpha A^{\gamma}$ [(1) this study, deposit area-mean volume, $\alpha = 30.60$, $\gamma = 1.12$; (2) this study, deposit area-deposit volume, $\alpha = 2.58$, $\gamma = 1.24$; (3) this study, total area-mean volume, $\alpha = 2.53$, $\gamma = 1.23$; (4) Legros (2002), Martian landslides, $\alpha = 0.20$, $\gamma = 1.43$; (5) Larsen et al. (2010), all landslides, $\alpha = 0.15$, $\gamma = 1.33$; (6) Larsen et al. (2010), bedrock landslides, $\alpha = 0.19$, $\gamma = 1.35$; (7) Larsen et al. (2010), soil landslides, $\alpha = 0.36$, $\gamma = 1.15$; (8) Legros (2002), volcanic rock avalanches, $\alpha = 1.27$, $\gamma = 1.15$; (9) Capra et al. (2002), debris avalanches, $\alpha = 30.60$, $\gamma = 1.12$; (10) Sosio, Crosta, and Hungr (2012), $\alpha = 2.60$, $\gamma = 0.86$; (11) Griswold and Iverson (2008), lahars, $\alpha = 0.01$, $\gamma = 1.45$; (12) Legros, 2002, debris flows, $\alpha = 0.01$, $\gamma = 1.32$; (13) Crosta et al. (2003), debris flows, $\alpha = 0.08$, $\gamma = 1.45$].

reworking of the deposits. Finally, the slope gradient of the depositional portion of the path can control the deposit elongation, but this is not a simple data to collect because of the local morphological variability of the depositional surfaces.

The comparison of volume versus area data for Martian and terrestrial landslides is shown in Figure 24. For a given volume, Martian rock avalanches spread over smaller areas with respect to terrestrial ones with a difference that decreases with increasing volume. As a consequence, Martian landslides are generally thicker than their terrestrial analogues. Furthermore, terrestrial landslide data are more dispersed than those for Martian landslides. This could be due to the more complex geometries of terrestrial landslides (i.e., more complex topographies with respect to the step-like ones typical of Martian landscapes). Moreover, the same approach has been consistently applied for volume estimate in this study, while different approaches for the determination of terrestrial landslide volumes have been used by different authors increasing the associated uncertainty in the estimate.

The power law relationships between volume and area have exponents ranging between 1.12 and 1.24 for Martian landslides (section 4.2) slightly deviating from a theoretical 1.5 value (3/2) for the case of self-similarity, which is typical of scale-independent frictional behavior. Notice that a Bingham fluid (assumed as a simple model of a non-Newtonian fluid behavior) tends to spread at constant thickness T independent of the initial volume and dependent only on the slope angle and the shear strength of the material. Thus, for a Bingham fluid, the volume $V = AT$ is independent of the volume itself. This implies a proportionality between volume V and spreading surface A, or an exponent 1.0. Thus, the values for the exponents found in this work suggest an intermediate rheology between a purely Bingham (exponent = 1) and a frictional behavior (exponent = 1.5). This could suggest an increasing role played by ice or ice-melt water in the mobilization and spreading of landslides.

The relationships plotted in Figure 24 show almost an order of magnitude of difference between Martian and terrestrial landslide areas for the same volume. Much larger differences occur with terrestrial debris flows and lahars (Crosta et al., 2003; Griswold & Iverson, 2008). Furthermore, terrestrial landslides seem less mobile (i.e., smaller area) for extremely large volumes (larger than 3×10^{11} m^3) with respect to Martian counterparts. This could be due to the small number of available terrestrial phenomena characterized by such large volumes with respect to those available for Mars.

Among the landslide geometrical characteristics, the degree of material evacuation from the source area is examined by considering the ratios of the scar area to the failure surface area and of the scar area to the deposit area. These ratios allow to draw some conclusions concerning the material properties (i.e., more or less abundant volatiles and presence of finer particles), the external energy inputs (e.g., impact cratering), and the consequent landslide mobility (i.e., long and short runout, partial or total evacuation of the source zone).

5.5. Landslide Mobility

The use of a large database allows us to perform a statistically sound study of mobility, expressed in terms of the H/L ratio between fall height H and runout L. In general, landslide mobility is observed to increase with the degree of confinement, in which case it appears to be associated to lateral levees, frontal runup, frontal confinement, and landslide front reflection. These conditions can be partially considered a result of the larger mobility. In fact, a larger mobility causes a stronger interaction of the moving mass and of its front with the opposite valley flank or other constraining features and morphologies. Then, confinement appears as another controlling factor for which it is difficult to discern between the cause or effect relationship.

On the other hand, an increase in mobility is observed for lateral and bilateral confinement. This is interesting because while our data are in line with field data for terrestrial rock avalanches, which indicate that confinement increases the mobility of rock avalanches (Nicoletti & Sorriso-Valvo, 1991), they appear partially in conflict with that suggested by small scale 1 g experiments (Shea & van Wyk de Vries, 2008). This could be explained by the fact that experiments fixed a channel width as it occurs in long channeled flows along narrow valleys. In case of large open areas, where self-channeling by deposition of lateral levees or presence of shallow confining features (e.g., other landslide deposits or small terraces) may occur, a longer runout (smaller *H*/*L* ratio) is observed possibly by the effect of these features in hampering an excessive landslide thinning.

Multiple lobes or finger-like deposits are associated to the most mobile landslides. As a consequence, this could provide evidence for a wetter condition or the presence of ice both within the landslide mass or along the paleotopographic surface over which spreading occurred. The fact that lower values of the *H*/*L* ratio are observed for landslide deposits with hummocky, hummocky striated, transversally striated, and stepped internal structures (see Figure S14 in the supporting information) could be attributed to the fact that these are features typical of landslide deposits affected by strong internal elongation (i.e., regime of internal extension) also during the depositional stage. An augmented landslide mobility is also associated to higher latitudes with particular evidence for the southern hemisphere. This observation could raise some clue about the possible effects of the presence of water or more probably ice within the destabilized mass or along the ground surface over which the landslide spreading took place.

A comparison of mobility between terrestrial and Martian landslides suggests that on average the latter are less mobile than their terrestrial counterparts as already observed in past studies (Crosta et al., 2015; Lucchitta, 1979; Lucchitta et al., 1992; McEwen, 1989). This lower mobility may be attributed to different factors among which the properties of the materials, the lower gravity of Mars with respect to the Earth, a different role of ice and/or water, and the morphological conditions of the area where they occurred. Landslides affecting volcanic edifices on Mars are characterized by long runouts as observed also for their terrestrial analogues (Sosio, Crosta, & Hungr, 2012).

Special landslide types are those associated with impact craters. Figure 21 shows that *H*/*L* values for these typologies (AOC, AIC, and IC) are the lowest ones. A working hypothesis to explain such a behavior could be that many of these landslides occurred in rock masses strongly weakened by the high-energy impacts or just after the major impact that could have melt most of the ice filling the voids or deposited in the regolith materials covering the Mars surface. For some of the landslides departing from the crater rim and propagating within large impact craters, the hypothesis of landslide occurrence contemporaneous to the crater formation seems less probable because most of the craters are characterized by smooth flat surfaces related to crater infilling. This phase of infilling must have required significant time, and the landslide material lays uncovered above the flat filling. In some special cases, however, mobility of the rock avalanches and flows was the result of the direct meteoroid impact in close proximity or along the slopes. Under such conditions, part of the impact energy was transferred directly to the slope material, which became destabilized and flowed along the slope.

5.6. Controlling Factors

Landslide occurrence is associated to controlling factors, distinguished in predisposing and triggering factors. While the former are determined by the previous geomorphological and geological history of the area, the latter represent the fast, time-dependent perturbation from quasistatic conditions that lead to the final collapse. On Earth, brecciated rocks, high relief, and steep sloping angle are predisposing factors of great importance. Triggering factors include seismic shaking, precipitation, and increase in groundwater circulation, singularly or in joint action. On Mars, predisposing factors such as the high relief in VM and at the crater rims are significant (Bigot-Cormier & Montgomery, 2007; Crosta et al., 2014) but may not have been enough for the final collapse. Some general conclusions concerning controlling factors can be inferred from the joint analysis of the inventory and some available data and models. While the same stability principles evidently rule landslide collapse on both Earth and Mars, there are important differences. In the following, first we consider the role of meteoroid impacts on some of the landslides, a triggering factor that has no obvious counterpart on Earth. Then, the role of groundwater and cryosphere is discussed using in conjunction the impact crater database by Robbins and Hynek (2012) and the Martian cryosphere model by Clifford et al. (2010).

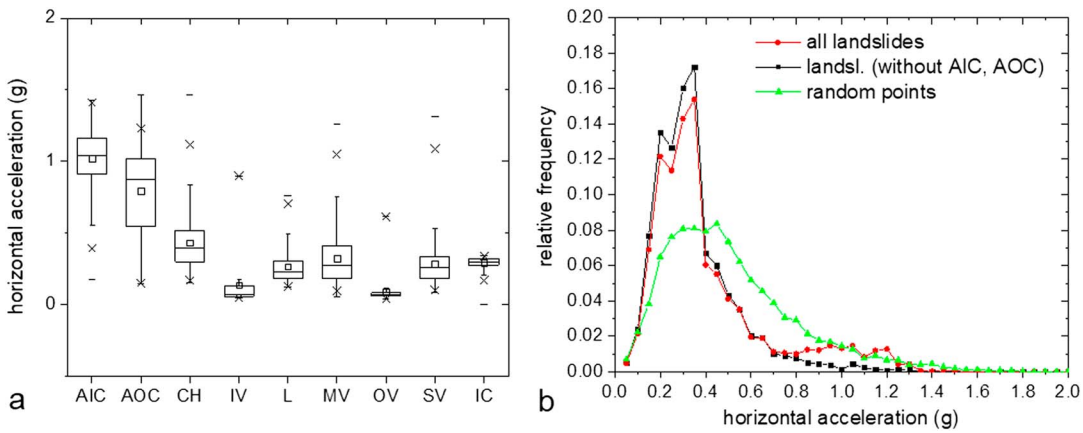

Figure 25. (a) Box and whiskers plot for the maximum horizontal accelerations computed at the landslide sites, by considering impacts generating craters in the 2–30 km diameter range; (b) relative frequency plot of the horizontal accelerations computed for landslides and for 10,000 randomly placed points within 45°S and 45°N.

5.6.1. Seismic Triggering From Meteoroid Impact

The seismicity induced by high-energy meteoric impacts on Mars may be a trigger for landslides. To test this hypothesis, we estimated the equivalent seismic magnitude from the kinetic energy of the impactor after Collins, Melosh, and Marcus (2005), based on the size of the craters reported in Robbins and Hynek (2012). Then, we calculated the horizontal acceleration using an attenuation law from Campbell (1981), and we assigned to each landslide scar the acceleration of all the crates lying within a distance of 200 km.

Considering the size of the landslides and assuming that smaller craters could not release enough energy to trigger such landslides, we limited the analysis to craters with a diameter larger than 2 km. Furthermore, we excluded craters with a diameter larger than 30 km, being these craters extremely rare and possibly associated to an age older than the landslides.

From the accelerations assigned to each landslide, we selected the maximum values, under the hypothesis that the most severe impact could have triggered the landslides. Values of horizontal acceleration at the scar location range from 0 to about 2 g. We observe a high level of acceleration associated to AOC and AIC, which are landslides interpreted, during mapping, as triggered by a crater-forming impacts. These results confirm the interpretation. For the other geographical settings, it is worth noting that the values of acceleration is lower for landslides outside of inside volcanoes, probably due to the lower density of craters in the Olympus Mons edifice.

To assess how seismic acceleration due to impact is suitable to be a trigger for Martian landslides, we compared the distribution of maximum acceleration at the scar location with the distribution of maximum acceleration calculated for 10,000 random points located over the surface of Mars, limiting the points within 45°S and 45°N, where landslides were mapped.

The acceleration at the scar locations are, in mean, lower than that at the random points, thus suggesting that landslides statistically do not tend to locate closer to craters with respect to random points (Figure 25a). This seems to exclude the seismic input as a main trigger of these landslides. Different for the landslides classified as AIC and AOC, which show values of acceleration significantly higher than the other landslides, these landslides are clearly recognizable in the frequency distribution (Figure 25b).

5.6.2. Ice and Groundwater Controls

The presence of ice and/or water at and below the ground surface could control the triggering and the spreading of landslides. Iced soils and rocks can be more resistant than dry ones because of the cementing effect of ice, but the strength could progressively decrease during thawing. Groundwater at depth can also decrease the stability of slopes favoring the triggering of landslides. As a consequence, it can be worth of interest the analysis of some of these factors for Martian landslides.

Different authors discuss the occurrence of evidence relatively to the presence of water and ice at different times on the Martian surface. From the presented landslide inventory here, it is possible to verify if there is any possible relationship between the landslide geometry and the cryosphere characteristics. To this

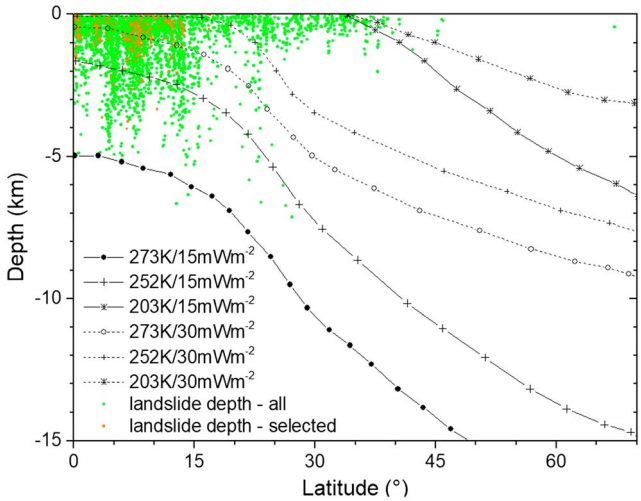

Figure 26. Depth of the water-ice cryosphere as determined by Clifford et al. (2010) at changing the latitude by assuming the groundwater freezing temperature (203 K, 252 K, and 273 K), the lithospheric heat flow (15 and 30 mW m^{-2}), and the thermal conductivity (0.1 W m^{-1} K^{-1}) of the 5 m superficial desiccated regolith. Green and red dots represent the height of the main scarp, for all the landslides, and the reconstructed depth of the failure surface, for the 222 selected landslides, respectively.

regard, as said above, landslides tend to disappear at high latitudes where glacial and periglacial forms and deposits become abundant.

Clifford et al. (2010) presented a model for the determination of the depth of the water-ice cryosphere at changing the latitude, the groundwater freezing temperatures, the lithospheric heat flow, and the thermal conductivity of the superficial desiccated regolith (defined as unconsolidated, porous volcanic, or sedimentary rock). Landslide main scarps, landslide thickness, depth of the basal landslide shear zone, and local relief can indicate the depth of a weaker zone or the thickness of a weaker layer. Starting from the Martian topographic data sets and from the landslide inventory, the maximum landslide scarp height for each landslide was computed. For the selected sample made of 222 landslides, the reconstructed basal failure planes allow to compute the maximum and mean landslide depth. The maximum depth is plotted in Figure 26 together with the limit curves of the depth of the water-ice cryosphere calculated by Clifford et al. (2010). It is possible to notice that all the points fall above the 273°K and 15 mW m^{-2} curve, where these values represent the assumed groundwater freezing temperature and the lithospheric heat flow, respectively. The position of the cryosphere basal surface is variable, but no landslide seems to go deeper than the maximum interface depth. This could potentially suggest the following: the presence of weaker material at the base of the cryosphere where ground ice is absent; the effect of groundwater positioned below the cryosphere base; and the damage caused by the ice formation. The maximum failure depths are located close to the equator or at low latitudes, but this is controlled very much by the distribution of available local relief (i.e., Noctis Labyrinthus, VM, and Margaritifer Terra) and slope gradient. Even if this does not lead to conclusive interpretations, the maximum age of the landslides (Early Amazonian) and the presence of ice can help at formulating some ideas about slope stability and factors controlling the runout of failed slopes (Crosta et al., 2017).

On the other hand, some shallow landslides typical of Noctis Labyrinthus and of VM could be associated to the instability affecting the desiccated regolith layer. Clifford et al. (2010) suggest the existence of a 0 to 5 m completely dry layer, underlain by one susceptible to desiccation and extending up to about 180 m. Hence, dry shallow slope instabilities could have occurred or the thin dry layer could have covered an icy surface that could have controlled the landslide runout (Crosta et al., 2018).

5.7. Comparison With Terrestrial: Dry, Glacial, and Volcanic

As said above, a first obvious difference between Martian and terrestrial landslides is the maximum volume involved in each mass flow. As consequence of the lower gravity field, the onset of instability on Mars requires higher headwalls than on Earth for similar slope angles, in order to develop the shear stress necessary to overcome friction and cohesion. The result is that landslides may often exceed volumes of the order 1,000 km^3 in VM and an astounding 10^6 km^3 for the Olympus Mons rock avalanches ("aureoles"; De Blasio, 2011b). These figures have to be compared with a value of 20 km^3 of the largest terrestrial subaerial rock avalanche and 3,000 km^3 of the largest submarine landslide. Note that both for terrestrial and Martian landslide deposits, the apparent friction *H*/*L* decreases as a function of the volume. Therefore, the largest landslides on Mars travel with apparent friction of only 0.1 or even less. For the landslides of Olympus Mons, this apparent friction is severely reduced to 0.02.

It is also interesting to perform a morphological comparison between terrestrial and Martian landslides. The first, most obvious similarity is the presence of grooves ("furrows") longitudinal to flow on most Martian landslides (see images in Figures S10a, S10c, S10e, S10i, S10n, S11a, S11e, S11d, and S11f). Such furrows are much similar to the ones observable on the surface of terrestrial landslides traveling on glaciers. Figures 27a–27h show some examples from Alaskan glaciers. These features are also present where multiple events occurred resulting in superposed deposits (Figures S10a and S11d). Note that in the Alaskan examples of Figures 27a–27h, the landslide mass tends to spread along a wide area, similar to a viscous fluid, a

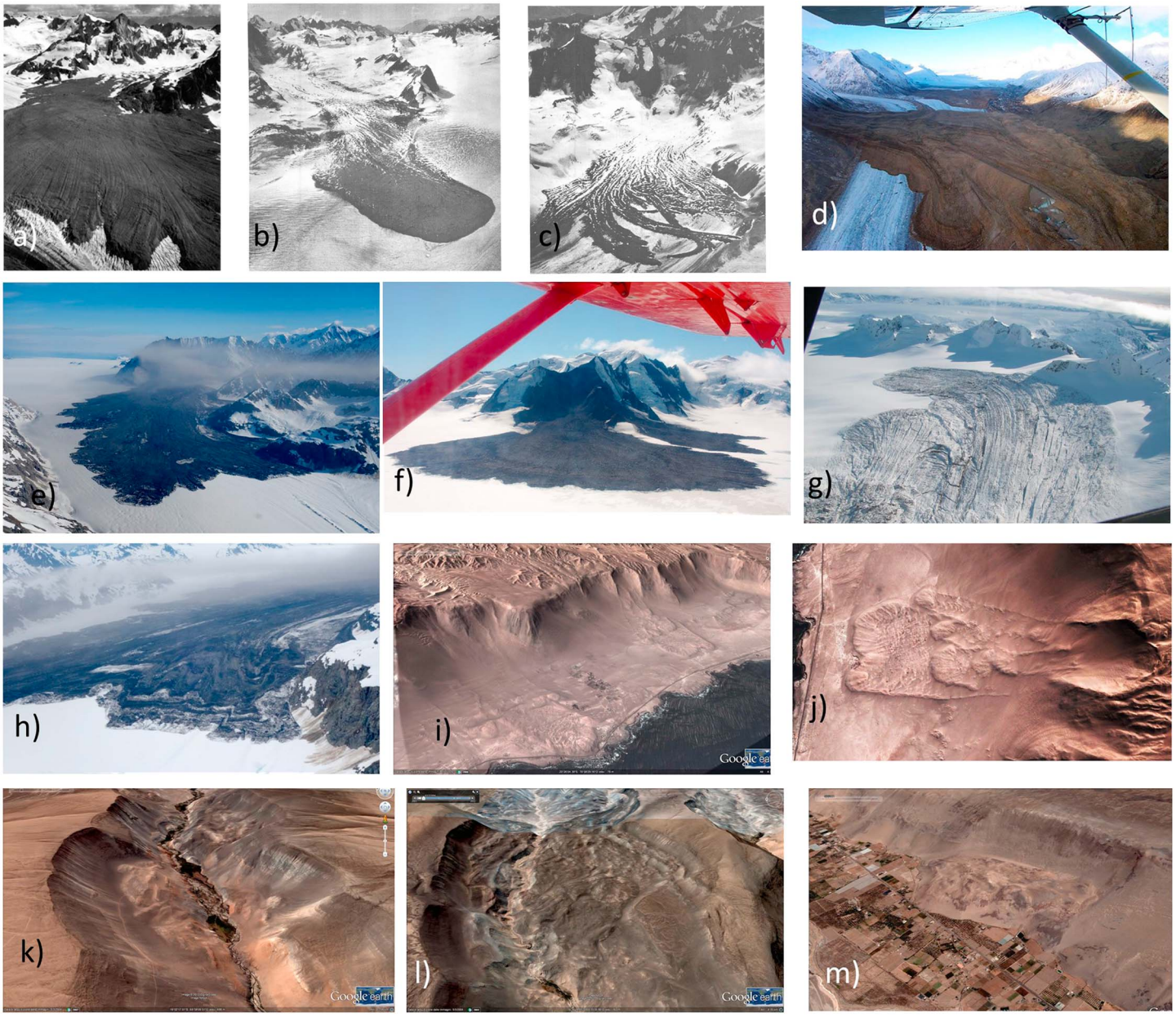

Figure 27. Examples of terrestrial analogs for some of the Martian landslide types. (a–h) Rock avalanches on glaciers; (i, j) rock avalanches in desertic terrain; (k–m) slump-spreading in desertic terrain. (a) 1964 rockslide avalanche on Sherman Glacier (Alaska, photo A. Post; Post, 1967). The debris displays flowlines and terminal digitate lobes and no marginal dust layer. (b) 1964 Allen rockslide avalanche 4 (Alaska photo A. Post; Post, 1967). (c) 1964 Allen Glacier rockslide avalanche 1 (Alaska photo A. Post; Post, 1967). (d) Rock avalanche deposit on the Black Rapids Glacier (photo by Rod March, USGS). Denali Fault Earthquake, *M*7.9, 3 November 2002. (e) Lamplugh Glacier, Glacier Bay National Park, 28 June 2016 (courtesy of Paul Swanstrom/Mountain Flying Service). (f) Bagley Ice Field, Alaska, 2015 (courtesy of Martin Truffer/Glacier Adventures). (g) Mount La Perouse rock avalanche, southeastern Alaska on 16 February 2014 (photo courtesy of FlyDrake Haines Alaska). (h) View of the front of the Lamplugh Glacier rock avalanche, Glacier Bay National Park, 28 June 2016 (courtesy of Paul Swanstrom/Mountain Flying Service). Festoon-like deposits made of landslide material and bulldozed snow and ice are visible. (i, j) Iquique, Atacama Desert, northern Chile, cluster of rock avalanche along the Pacific coast (from Google Earth™). (k, l, m) Northern Chile, Atacama Desert, large slump-spreading landslides. Compare to Figures 3, 4, S10, and S11.

behavior also seen in many of the landslides falling onto a flat area (Figures 3e, 3g, and 3h) especially inside craters and onto flat regions of VM (Figures S10 and S11). This similarity led Lucchitta (1979) and De Blasio (2011a) to invoke glacial conditions at the base of the VM, where most of such grooved landslides are observed. In some cases, fluted and streamlined morphologies depart from the front of these deposits suggesting the possible release of meltwater generated during the landslide motion. While some massive landslides preserve a frontal bulge (Figures S10c, S10e, S10m, 4a–4d, 27a, and 27b), thinner landslides tend

to split up in digitations, each following the trajectory induced by the local gradient and at times intersecting each other (Figure 27d). Similar digitations are visible also in Martian examples (Figures 3, 4, S10d, S10e, and S11e). Interestingly, rock avalanche and slump-flows with features similar to the Martian ones (Figures 4, 6b, 6c, and S9) have been recognized in one of the driest regions in the world (Figures 27i to 6m, Atacama desert in Northern Chile and Southern Peru; Crosta et al., 2018) as well as in other regions with different environmental conditions (e.g., Blackhawk landslide, southern California, Shreve, 1968; Bairaman landslide, Papua New Guinea, King, Loveday, & Schuster, 1989; sagging and large deep-seated gravitational slope instabilities, European Alps, Crosta, Frattini, & Agliardi, 2013; Sherman Glacier, Alaska, Shreve, 1966; Black Rapids, Alaska, Jibson et al., 2006; Shugar et al., 2012; Sosio et al., 2008). As a consequence, considering the different types of morphological features typical of the Martian landslides and of the long time span over which landslides occurred, no unique set of environmental conditions can be directly associated to them. Other similarities between terrestrial and Martian landslides include the possibility of a bulgy front in relief compared to the body (compare, e.g., the Martian examples of Figures 4e and S9f–S9i against the terrestrial ones in Figure 27j), tongue-like front (examples in Figure 4 versus Figures 27a–27h), diverging striations at the front (compare Figure 3g with Figures 27g, 27i, and 27j), transversal to flow ridges (compare Figures 27d and 27j to Figures 27j, S10f, S10m, and S11f), festoon-like ridges (compare Figures 27d, 27f, and 27h to Figures 4a, S10a, S10i, S11a, and S11f), bulging whirl-like features along the lateral deposit boundaries (compare Figures 27d, 27i, 27j, S10h, and S10m to Figures 3g and 4d), and the possibility of multiple failure resulting in superimposition of landslide deposits (Figures 27j and S9i show notable similarities).

Finally, a special class of phenomena is the one associated to instability of volcanic edifices (Sosio, Crosta, Chen, et al., 2012). The collapse of large portions of the volcanoes is at the origin of enormous rock avalanches (1–40 km^3) with long runout (1–100 km) and extreme areal extent (up to 1,500 km^2), complex deposit morphologies and internal structures, and presence of large Toreva blocks (e.g., Dufresneo et al., 2010; Shea & van Wyk de Vries, 2008; Wadge, Francis, & Ramirez, 1995). These phenomena are among the most mobile on Earth and seem to share some common features (e.g., elongated flow-like lobes, apron-like fans, hummocky deposits with longitudinal shear bands, compressive ridges, flow reflection, and diversion) with Martian mass movements both in association to volcanic (e.g., Olympus Mons) and nonvolcanic edifices.

6. Conclusions

In this paper, the first global Mars landslide database, going well beyond the number of mapped landslides in previous studies, is presented. The quality and quantity of landslide data in the VM area, in the neighboring valleys, and chaos have been strongly improved. Moreover, the database was extended beyond the limits of the areas investigated so far to regions seldom considered in the analysis on Martian landslides. Novel landslide data have been reported especially inside the craters at high northern or southern latitudes. Two new landslide classes are proposed, those characterized by Toreva-like blocks, with extreme front runout, and those directly associated to meteoroid impact. In addition, the study of landslide typologies has been improved compared to previous data and extended to include landslide types not previously recognized. A total of 3,118 landslides have been mapped as polygons, attributing to them a series of relevant properties including geometrical characteristics, landslide type, internal subdivision of the landslides, typical deposit characteristics, and mutual relationships between conterminous deposits.

The inventory covers a landslide area interval of about seven orders of magnitude and can be considered complete for landslides down to an area of about 10^6 m^2. The mapping was completed using all the available information and images available on Google Earth and on Mars missions image repositories, while elevations data were based on MOLA and HRSC topographic databases. Reconstruction of failure surfaces of some 222 landslides allowed the computation of volume to area relationships improving the understanding of landslide behavior. Because of its size, the database is robust enough to describe statistical relationships of Martian landslides, and the most significant, but by no means the only ones, of these relationships are presented and discussed. In particular, the geographical distribution, the effect of local morphology and degree of confinement, the magnitude frequency curves and their dependence on geographical location, morphology, and environment, and degree of confinement, are examined together with similarities to terrestrial landslides. These, together with available databases and models, allow us to draw some conclusions about possible controlling factors on landslide initiation, runout, and paleoenvironmental conditions at the

time of occurrence. The analysis of landslide versus impact crater distributions suggests that meteoroid impacts probably had only a limited influence on landslide triggering. Comparing landslide depth with results of cryosphere models supports the hypothesis that ice could have played a relevant role in slope stability control and in some sectors, where more superficial failures occur, this was affecting the most superficial and desiccated regolith layer.

One direction of future research is a more comprehensive landslide dating by crater counting, which will put the database in a planetary evolutionary context. Clearly, because one single dating requires several hours of working time, this task will require a major effort and can be accomplished only for a few landslides. All landslides dating from previous publications give Amazonian ages, with only a relatively small Hesperian component (the record of the oldest documented landslides is around 3.5 Ga; Hager & Schedl, 2017; Quantin, Allemand, Mangold, et al., 2004). Our own preliminary dating of some landslides also show Amazonian ages. Landslides in the outflow channels are poorly documented compared to the more studied VM, even though such channels are characterized by high relief (albeit not comparable to VM) and steep slope. We are studying the distribution of such landslides in Shalbatana and Kasei Valles as a function of the position along the channel and of age.

Acknowledgments
We acknowledge the four anonymous reviewers and especially to N. Warner for the constructive comments. The authors of the terrestrial landslide photographs are also acknowledged. The study has been completed without any official project funding. The geodatabase in its full format will be made fully available through the authors' website. The geodatabase in a point-like format is available in the electronic material linked to this publication.

References

Andrews-Hanna, J. C. (2012a). The formation of Valles Marineris: 1. Tectonic architecture and the relative roles of extension and subsidence. *Journal of Geophysical Research*, *117*, E03006. https://doi.org/10.1029/2011JE003953

Andrews-Hanna, J. C. (2012b). The formation of Valles Marineris: 2. Stress focusing along the buried dichotomy boundary. *Journal of Geophysical Research*, *117*, E04009. https://doi.org/10.1029/2011JE003954

Andrews-Hanna, J. C. (2012c). The formation of Valles Marineris: 3. Trough formation through super-isostasy, stress, sedimentation, and subsidence. *Journal of Geophysical Research*, *117*, E06002. https://doi.org/10.1029/2012JE004059

Barlow, N. G., & Perez, C. B. (2003). Martian impact crater ejecta morphologies as indicators of the distribution of subsurface volatiles. *Journal of Geophysical Research*, *108*(E8), 5085. https://doi.org/10.1029/2002JE002036

Barsch, D. (1996). *Rock glaciers. Indicators for the present and former geoecology in high mountain environments*. Berlin: Springer.

Bigot-Cormier, F., & Montgomery, D. R. (2007). Valles Marineris landslides: Evidence for a strength limit to Martian relief? *Earth and Planetary Science Letters*, *260*, 179–186.

Brunetti, M. T., Guzzetti, F., Cardinali, M., Fiorucci, F., Santangelo, M., Mancinelli, P., et al. (2014). Analysis of a new geomorphological inventory of landslides in Valles Marineris, Mars. *Earth and Planetary Science Letters*, *405*, 156–168.

Bulmer, M. H. K. (2012). Landslides on other planets. In J. J. Clague & D. Stead (Eds.), *Landslides: Types, mechanisms and modelling* (pp. 393–408). Cambridge: Cambridge University Press.

Campbell, K. W. (1981). Near-source attenuation of peak horizontal acceleration. *Bulletin of the Seismological Society of America*, *71*(6), 2039–2070.

Carr, M. H. (1996). Channels and valleys on Mars: Cold climate features formed as a result of a thickening cryosphere. *Planetary and Space Science*, *44*(11), 1411–1423.

Capra, L., Macías, J. L., Scott, K. M., Abrams, M., & Garduño-Monroy, V. H. (2002). Debris avalanches and debris flows transformed from collapses in the Trans-Mexican Volcanic Belt, Mexico - Behavior, and implications for hazard assessment. *Journal of Volcanology and Geothermal Research*, *113*(1–2), 81–110.

Clifford, S. M., Lasue, J., Heggy, E., Boisson, J., McGovern, P., & Max, M. D. (2010). Depth of the Martian cryosphere: Revised estimates and implications for the existence and detection of subpermafrost groundwater. *Journal of Geophysical Research*, *115*, E07001. https://doi.org/10.1029/2009JE003462

Colaprete, A., & Jakosky, B. M. (1998). Ice flow and rock glaciers on Mars. *Journal of Geophysical Research*, *103*(E3), 5897–5909.

Collins, G. S., Melosh, H. J., & Marcus, R. A. (2005). Earth impact effects program: A Web-based computer program for calculating the regional environmental consequences of a meteoroid impact on Earth. *Meteoritics & Planetary Science*, *40*(6), 817–840.

Crosta, G. B., Cucchiaro, S., & Frattini, P. (2003). Validation of semi-empirical relationships for the definition of debris-flow behavior in granular materials. In *Proceedings of the Third International Conference on Debris-Flow Hazards Mitigation: Mechanics, Prediction and Assessment, Davos, Switzerland* (pp. 821–831). Rotterdam: Millpress.

Crosta, G. B., De Blasio, F. V., De Caro, M., Volpi, G., Imposimato, S., & Roddeman, D. (2017). Modes of propagation and deposition of granular flows onto an erodible substrate: Experimental, analytical, and numerical study. *Landslides*, *14*(1), 47–68.

Crosta, G. B., De Blasio, F. V., & Frattini, P. (2018). Global scale analysis of Martian landslide mobility and paleoenvironmental clues. *Journal of Geophysical Research: Planets*, *123*. https://doi.org/10.1002/2017JE005398

Crosta, G. B., De Blasio, F. V., Locatelli, M., Imposimato, S., & Roddeman, D. (2015). Landslides falling onto a shallow erodible substrate or water layer: an experimental and numerical approach. In *IOP Conference Series: Earth and Environmental Science* (Vol. 26, No. 1, p. 012004). IOP.

Crosta, G. B., Frattini, P., & Agliardi, F. (2013). Deep seated gravitational slope deformations in the European Alps. *Tectonophysics*, *605*, 13–33.

Crosta, G. B., Frattini, P., & Valbuzzi, E. (2013). A new inventory of Martian landslides. LPI Contributions 1719, 2283 (ext. abstract).

Crosta, G. B., Utili, S., De Blasio, F.V., & Castellanza, R. (2013). Landslides in Valles Marineris, Mars: An analysis of failure types to ascertain rock mass properties, Predisposing and Triggering Factors. 44th Lunar and Planetary Science Conference (2013), Abstract 1624.

Crosta, G. B., Utili, S., De Blasio, F. V., & Castellanza, R. (2014). Reassessing rock mass properties and slope instability triggering conditions in Valles Marineris, Mars. *Earth and Planetary Science Letters*, *338*, 329–343.

Cruden, D. M., & Varnes, D. J. (1996). Landslide types and processes. In A. K. Turner & R. L. Schuster (Eds.), *Landslides: Investigation and mitigation*, *Transportation research board, Special Report* (Vol. 247, pp. 36–75). Washington, DC: US National Research Council.

De Blasio, F. V. (2011a). Landslides in Valles Marineris (Mars): A possible role of basal lubrication by sub-surface ice. *Planetary and Space Science*, *59*, 1384–1392. https://doi.org/10.1016/j.pss.2011.04.015

De Blasio, F. V. (2011b). The aureole of Olympus Mons (Mars) as the compound deposit of submarine landslides. *Earth and Planetary Science Letters*, *312*, 126–139.

Di Achille, G., & Hynek, B. M. (2010). Ancient ocean on Mars supported by global distribution of deltas and valleys. *Nature Geoscience*, *3*, 459–463.

Dufresne, A., Salinas, S., & Siebe, C. (2010). Substrate deformation associated with the Jocotitlán edifice collapse and debris avalanche deposit, Central México. *Journal of Volcanology and Geothermal Research*, *197*(1–4), 133–148.

Erismann, T. H., & Abele, G. (2001). *Dynamics of Rockslides and Rockfalls* (pp. 107–144). Berlin: Springer. https://doi.org/10.1007/978-3-662-04639-5

Frattini, P., & Crosta, G. B. (2013). The role of material properties and landscape morphology on landslide size distributions. *Earth and Planetary Science Letters*, *361*, 310–319.

Frattini, P., Crosta, G.B., De Blasio, F.V., Castellanza, R., Utili, S., & Lucas, A. (2014). Crater shock damage zone and landslide size distribution in Valles Marineris, Mars 45th Lunar and Planetary Science Conference (2014), Abstract 2024.

Grindrod, P. M., & Warner, N. H. (2014). Erosion rate and previous extent of interior layered deposits on Mars revealed by obstructed landslides. *Geology*, *42*(9), 795–798.

Griswold, J. P., & Iverson, R. M. (2008). Mobility statistics and automated hazard mapping for debris flows and rock avalanches (ver. 1.1, April 2014): U.S. Geological Survey Scientific Investigations Report 2007-5276 (59 pp.).

Hager, A., & Schedl, A. D. (2017). Classification and ages of landslides within Valles Marineris. In Lunar and Planetary Science Conference (Vol. 48) 48th Lunar and Planetary Science Conference, held 20–24 March 2017, at The Woodlands, Texas. LPI Contribution No. 1964, id.2076.

Hamilton, S. J., & Whalley, W. B. (1995). Rock glacier nomenclature: A re-assessment. *Geomorphology*, *14*, 73–80.

Harrison, K. P., & Grimm, R. E. (2003). Rheological constraints on Martian landslides. *Icarus*, *163*(2), 347–362.

Hartmann, W. K., & Werner, S. C. (2010). Martian cratering 10. Progress in use of crater counts to interpret geological processes: Examples from two debris aprons. *Earth and Planetary Science Letters*, *294*(3), 230–237.

Hubbard, B., Souness, C., & Brough, S. (2014). Glacier-like forms on Mars. *The Cryosphere*, *8*(6), 2047–2061. https://doi.org/10.5194/tc-8-2047-2014

Hungr, O., Leroueil, S., & Picarelli, L. (2014). The Varnes classification of landslide types, an update. *Landslides*, *11*(2), 167–194.

Jibson, R. W., Harp, E. L., Schulz, W., & Keefer, D. K. (2006). Large rock avalanches triggered by the *M* 7.9 Denali fault, Alaska, earthquake of 3 November 2002. *Engineering Geology*, *83*, 144e160.

Johnsson, A., Reiss, D., Hauber, E., Hiesinger, H., & Zanetti, M. (2014). Evidence for very recent melt-water and debris flow activity in gullies in a young mid-latitude crater on Mars. *Icarus*, *235*, 37–54.

Kargel, J. S. (2004). *Mars—A warmer, wetter planet*. Berlin: Springer Science & Business Media.

Katz, O., & Aharonov, E. (2006). Landslides in vibrating sand box: What controls types of slope failure and frequency magnitude relations? *Earth and Planetary Science Letters*, *247*(3–4), 280–294. https://doi.org/10.1016/j.epsl.2006.05.009

King, J., Loveday, I., & Schuster, R. L. (1989). The 1985 Bairaman landslide dam and resulting debris flow, Papua New Guinea. *Quarterly Journal of Engineering Geology*, *22*(4), 257–270. https://doi.org/10.1144/GSL.QJEG.1989.022.04.02

Lanza, N. L., Meyer, G. A., Okubo, C. H., Newsom, H. E., & Wiens, R. C. (2010). Evidence for debris flow gully formation initiated by shallow subsurface water on Mars. *Icarus*, *205*(1), 103–112.

Larsen, I. J., Montgomery, D. R., & Korup, O. (2010). Landslide erosion controlled by hillslope material. *Nature Geoscience*, *3*(4), 247–251.

Laskar, J., Correia, A. C. M., Gastineau, M., Joutel, F., Levrard, B., & Robutel, P. (2004). Long term evolution and chaotic diffusion of the insolation quantities of Mars. *Icarus*, *170*(2), 343–364.

Legros, F. (2002). The mobility of long-runout landslides. *Engineering Geology*, *63*(3–4), 301–331.

Lucas, A., Mangeney, A., & Ampuero, J. P. (2014). Frictional velocity-weakening in landslides on Earth and on other planetary bodies. *Nature Communications*, *5*, 3417.

Lucas, A., Mangeney, A., Mège, D., & Bouchut, F. (2011). Influence of the scar geometry on landslide dynamics and deposits: Application to Martian landslides. *Journal of Geophysical Research*, *116*, E10001. https://doi.org/10.1029/2011JE003803

Lucchitta, B. K. (1979). Landslides in Vallis Marineris, Mars. *Journal of Geophysical Research*, *84*, 8097–8113.

Lucchitta, B. K. (1987). Valles Marineris, Mars: Wet debris flows and ground ice. *Icarus*, *72*(2), 411–429.

Lucchitta, B. K., McEwen, A. S., Clow, G. D., Geissler, P. E., Singer, R. B., Schultz, R. A., & Squyres, S. W. (1992). The canyon system on Mars. In H. H. Kiefer, et al. (Eds.), *Mars* (pp. 453–492). Tucson, AZ: University of Arizona Press.

Malamud, B. D., Turcotte, D. L., Guzzetti, F., & Reichenbach, P. (2004). Landslide inventories and their statistical properties. *Earth Surface Processes and Landforms*, *29*, 687–711.

Malin, M. C., Bell, J. F. III, Cantor, B. A., Caplinger, M. A., Calvin, W. M., Clancy, R. T., et al. (2007). Context camera investigation on board the Mars reconnaissance orbiter. *Journal of Geophysical Research*, *112*, E06S04. https://doi.org/10.1029/2006JE002808

Malin, M. C., & Edgett, K. S. (2000). Evidence for recent groundwater seepage and surface runoff on Mars. *Science*, *288*(5475), 2330–2335.

McEwen, A. S. (1989). Mobility of large rock avalanches: Evidence from Valles Marineris, Mars. *Geology*, *17*, 1111–1114.

McEwen, A. S., Dundas, C. M., Mattson, S. S., Toigo, A. D., Ojha, L., & Wray, J. J. (2013). Recurring slope lineae in equatorial regions of Mars. *Nature Geoscience*, *7*, 53–58.

Mège, D., & Bourgeois, O. (2011). Equatorial glaciations on Mars revealed by gravitational collapse of Valles Marineris wallslopes. *Earth and Planetary Science Letters*, *310*(3), 182–191.

Neuffer, D. P., & Schultz, R. A. (2006). Mechanisms of slope failure in Valles Marineris, Mars. *Quarterly Journal of Engineering Geology and Hydrogeology*, *39*(3), 227–240.

Neukum, G., Jaumann, R., & the HRSC Co-Investigator and Experiment Team (2004). HRSC: The high resolution stereo camera of Mars Express. In A. Wilson (Ed.), *Mars Express: The scientific payload* (pp. 17–35). Noordwijk, Netherlands: ESA.

Nicoletti, P. G., & Sorriso-Valvo, M. (1991). Geomorphic controls of the shape and mobility of rock avalanches. *Geological Society of America Bulletin*, *103*(10), 1365–1373.

Platz, T., Michael, G., Tanaka, K. L., Skinner, J. A., & Fortezzo, C. M. (2013). Crater-based dating of geological units on Mars: Methods and application for the new global geological map. *Icarus*, *225*(1), 806–827.

Post, A. (1967). Effects of the March 1964 Alaska earthquake on glaciers. *U.S. Geological Survey Professional Paper, 544-D*, 42.

Quantin, C., Allemand, P., & Delacourt, C. (2004). Morphology and geometry of Valles Marineris landslides. *Planetary and Space Science*, *52*(11), 1011–1022.

Quantin, C., Allemand, P., Mangold, N., & Delacourt, C. (2004). Ages of Valles Marineris (Mars) landslides and implications for canyon history. *Icarus*, *172*, 555–572.

Reiche, P. (1937). Toreva block—A distinctive landslide type. *Journal of Geology*, *45*, 538–540.
Robbins, S. J., & Hynek, B. M. (2012). A new global database of Mars impact craters ≥ 1 km: 1. Database creation, properties, and parameters. *Journal of Geophysical Research*, *117* E05004. https://doi.org/10.1029/2011JE003966
Scheidegger, A. E. (1973). On the prediction of the release and velocity of catastrophic rockfalls. *Rock Mechanics*, *5*, 231–236.
Schultz, R. A. (2002). Stability of rock slopes in Valles Marineris, Mars. *Geophysical Research Letters*, *29*(19), 1932. https://doi.org/10.1029/2002GL015728
Shaller, R. (1991). Analysis and implications of large Martian and terrestrial landslides (PhD thesis, 586 pp.). CA: California Institute of Technology.
Shea, T., & van Wyk de Vries, B. (2008). Structural analysis and analogue modeling of the kinematics and dynamics of rockslide avalanches. *Geosphere*, *4*(4), 657–686.
Shreve, R. L. (1966). Sherman landslide, Alaska. *Science*, *154*(3757), 1639–1643.
Shreve, R. L. (1968). *The Blackhawk landslide. Geological Society of America, Special Paper, 108*, 47.
Shugar, D. H., Rabus, B. T., Clague, J. J., & Capps, D. M. (2012). The response of Black Rapids Glacier, Alaska, to the Denali earthquake rock avalanches. *Journal of Geophysical Research*, *117*, F01006. https://doi.org/10.1029/2011JF002011
Smith, D. E., Zuber, M. T., Solomon, S. C., Phillips, R. J., Head, J. W., Garvin, J. B., et al. (1999). The global topography of Mars and implications for surface evolution. *Science*, *284*(5419), 1495–1503.
Sosio, R., Crosta, G. B., Chen, J. H., & Hungr, O. (2012). Modelling rock avalanche propagation onto glaciers. *Quaternary Science Reviews*, *47*, 23–40.
Sosio, R., Crosta, G. B., & Hungr, O. (2008). Complete dynamic calibration for the Thurwieser rock avalanche (Italian Central Alps). *Engineering Geology*, *100*, 11–26.
Sosio, R., Crosta, G. B., & Hungr, O. (2012). Numerical modeling of debris avalanche propagation from collapse of volcanic edifices. *Landslides*, *9*(3), 315–334.
Souness, C., Hubbard, B., Milliken, R. E., & Quincey, D. (2012). An inventory and population-scale analysis of Martian glacier-like forms. *Icarus*, *217*(1), 243–255.
Stark, C. P., & Guzzetti, F. (2009). Landslide rupture and the probability distribution of mobilized debris volumes. *Journal of Geophysical Research*, *114*, F00A02. https://doi.org/10.1029/2008JF001008
Stucky de Quay, G., & Grindrod, P. M. (2014). A complete catalogue of landslides in Valles Marineris, Mars. In Lunar and Planetary Science Conference (Vol. 45, p. 1601).
Sullivan, R., Thomas, P., Veverka, J., Malin, M., & Edgett, K. S. (2001). Mass movement slope streaks imaged by the Mars Orbiter Camera. *Journal of Geophysical Research*, *106*(E10), 23,607–23,633. https://doi.org/10.1029/2000JE001296
Tanaka, K. L. (1999). Debris-flow origin for the Simud/Tiu deposit on Mars. *Journal of Geophysical Research*, *104*(E4), 8637–8652.
Tanaka, K. L., Skinner, J. A., Dohm, J. M., Irwin, R. P. III, Kolb, E. J., Fortezzo, C. M., et al. (2014). Geologic map of Mars. USGS Scientific Investigations Map 3292.
Ten Brink, U. S., Barkan, R., Andrews, B. D., & Chaytor, J. D. (2009). Size distributions and failure initiation of submarine and subaerial landslides. *Earth and Planetary Science Letters*, *287*(1), 31–42.
Utili, S., & Crosta, G. B. (2011). Modeling the evolution of natural cliffs subject to weathering: 1. Limit analysis approach. *Journal of Geophysical Research*, *116*, F01016. https://doi.org/10.1029/2009JF001557
Varnes, D. J. (1978). Slope movement types and processes. In R. L. Schuster & R. J. Krizek (Eds.), *Special Report 176: Landslides: Analysis and Control* (pp. 11–33). Washington, DC: Transportation and Road Research Board, National Academy of Science.
Wadge, G., Francis, P. W., & Ramirez, C. F. (1995). The Socompa collapse and avalanche event. *Journal of Volcanology and Geothermal Research*, *66*, 309–336.
Warner, N. H., Gupta, S., Calef, F., Grindrod, P., Boll, N., & Goddard, K. (2015). Minimum effective area for high resolution crater counting of Martian terrains. *Icarus*, *245*, 198–240.
Watkins, J. A., Ehlmann, B. L., & Yin, A. (2015). Long-runout landslides and the long-lasting effects of early water activity on Mars. *Geology*, *43*, 107–110. https://doi.org/10.1130/G36215.1
Weiss, D. K., & Head, J. W. (2013). Formation of double-layered ejecta craters on Mars: A glacial substrate model. *Geophysical Research Letters*, *40*, 3819–3824. https://doi.org/10.1002/grl.50778
Whalley, W. B., & Azizi, F. (2003). Rock glaciers and protalus landforms: Analogous forms and ice sources on Earth and Mars. *Journal of Geophysical Research*, *108*(E4), 8032. https://doi.org/10.1029/2002JE001864
Yin, A. (2012). Structural analysis of the Valles Marineris fault zone: Possible evidence for large-scale strike-slip faulting on Mars. *Lithosphere*, *4*(4), 286–330.